Received 16 November 2024; revised 12 December 2024; accepted 12 December 2024. Date of publication 17 December 2024; date of current version 22 January 2025.

Digital Object Identifier 10.1109/OJCOMS.2024.3519314

Post-Earthquake Network Restoration: Statistical Seismic Road Closure Prediction and Efficient MDRU Routing

AHMET ENES DURANAY [1] (Graduate Student Member, IEEE), XHELJA KODHELI [1] (Graduate Student Member, IEEE), AMR M. ABDELHADY [2] (Senior Member, IEEE), ABDULKADIR CELIK [2] (Senior Member, IEEE), AHMED M. ELTAWIL [2] (Senior Member, IEEE), AND HÜSEYIN ARSLAN [1] (Fellow, IEEE)

[1] Electrical and Electronics Engineering, School of Engineering and Natural Sciences, Istanbul Medipol University, 34810 Istanbul, Türkiye
[2] Computer Electrical, and Mathematical Science and Engineering Division, King Abdullah University of Science and Technology, Thuwal 23955, Saudi Arabia

CORRESPONDING AUTHOR: A. E. DURANAY (e-mail: aeduranay@medipol.edu.tr)

ABSTRACT Post-earthquake scenarios have brought connectivity challenges to the forefront of research in recent years. Particularly, the randomness and large-scale of road and telecom network infrastructure damage within the aftermath hinders communications coverage restoration during the most critical hours when lives are at stake. This paper proposes a seismic-based post-earthquake city and cellular network model to statistically predict the status of road closures and base station failures based on fundamental earthquake measurements. The presented model considers a generic Manhattan grid-based city model, with buildings featuring random heights. In addition, it quantifies the probability of building collapse and the consequent probability of road closure which accounts for the random debris nature. Moreover, the model accounts for the dependencies between the debris width, height, and the relative location with respect to the earthquake epicenter. Furthermore, a routing algorithm for movable and deployable resource units (MDRUs) that exploits the derived statistical model is proposed to ensure that MDRUs are efficiently deployed and connectivity is restored swiftly. The proposed routing algorithm is extensively tested over a large set of simulation scenarios depicting different earthquake magnitudes and was shown to provide up to 31% traveling time reduction compared to a blind distance-based approach. Finally, the conducted simulations showed the effectiveness of the proposed MDRUs deployment approach in restoring the communications coverage from a signal-to-interference plus noise ratio perspective in the majority of the considered locations.

INDEX TERMS Post-earthquake network model, building collapse probability, road blockage probability, MDRU routing algorithm, Dijkstra.

I. INTRODUCTION

NATURAL disasters, such as hurricanes, earthquakes, floods, and tsunamis, bring about environmental devastation, immense economic losses, and unpredictable fatalities. While disaster prevention is impossible, effective post-disaster management and recovery are paramount, and studied for various disasters from different perspectives in the literature [1]. Examples include search and rescue operations using Internet of Things (IoT)-oriented technologies in flood scenarios [2], rapid response strategies in pandemics utilizing sixth-generation (6G) wireless technologies [3], and a rescue information system implemented with Mobile Ad-hoc Networks (MANETs) in earthquake scenarios [4].

Current network infrastructure lacks adequate redundancy, and recent calamities have shown the vulnerability of wireless networks [5]. The criticality of the first post-disaster hours requires a rapid wireless connectivity restoration solution to aid the first responders in carrying out the needed rescue operations [6]. This was evident in the recent Kahramanmaraş Earthquakes (Pazarcık and Elbistan) in 2023, which ranked at the top in terms of casualties and severity [7].

In the Kahramanmaraş Earthquake doublet, physical damage or power outages rendered base stations (BSs) inoperable, leading to communication breakdowns; while the BSs in towers were less affected, the BSs mounted on buildings' rooftops, heavily used in cities, went out of service due to the buildings' collapse [8]. Repairing minor BS damage and delivering fuel for BS generators were delayed, and commissioning movable and deployable resource units (MDRUs) faced obstacles due to road blockages caused by debris. These network coverage and capacity shortages, in addition to hindering individual and institutional connectivity, disrupted search and rescue efforts, caused requests for help from people under the wreckage not to be received, and contributed to a higher loss of life [9].

When terrestrial infrastructure is damaged, repairing (if possible) or terrestrial ad-hoc solutions are preferable before jumping to other options, such as aerial base stations (ABSs). The work in [10] proposes using MDRUs, essentially vehicle-mounted base stations, as a comprehensive solution to meet user needs in disaster recovery scenarios. This approach offers various advantages, such as quick deployment, high capacity, valuable disaster-time applications, and carrier-free usability. Additionally, MDRUs can be powered by different energy sources and can operate for up to five days without an external power supply [11]. Typically, a disaster-resilient network architecture based on MDRUs is introduced to reduce traffic congestion in disaster-affected areas and meet communication demands [12]. They also outlined a restoration process for post-disaster scenarios using MDRUs. Furthermore, an optimization strategy is presented to reduce the density of MDRUs required for constructing the emergency communication network [13]. In [14], the novelty lies in integrating spectrum and energy efficiencies, resulting in the creation of a novel metric termed spectrum-energy efficiency for the disaster scenario, where MDRUs are deployed. The authors introduced a topological scheme based on the top-k spectrum-efficient paths and outlined methods for optimizing the value of k.

As the recovery of terrestrial networks in disaster-affected areas is sometimes unattainable or time-consuming due to road blockages, many studies in the literature have concentrated on alternatives, such as utilizing aerial networks serving as flying BSs. In [15], the authors presented an optimization-based approach for unmanned aerial vehicle (UAV)-aided disaster communications. A novel stochastic geometry framework is proposed in [16], which combines terrestrial and aerial networks with ad-hoc BSs, showcasing the effectiveness of vertical heterogeneous network (VHetNet) in emergency scenarios. In [17], the authors proposed the utilization of reconfigurable intelligent surfaces (RIS) in such scenarios and provided estimates of the average and local coverage probabilities of an aerial reconfigurable intelligent surfaces (ARIS)-assisted wireless network.

After all, we are facing a post-disaster management scenario where many solutions exist, including terrestrial networks and ABSs [18]. The prospect of integrating ABSs into wireless networks is enticing due to its numerous benefits, but it also presents challenges. The primary concerns when using ABSs as network infrastructure include their limited energy supply in the sense of network service availability and the lack of coordination with the terrestrial network regarding frequency usage and deployment location, which can lead to interference and worsen communication [19]. Therefore, employing terrestrial solutions is necessary during disaster times. Particularly in earthquakes, which have a devastating impact on infrastructure collapse, it is important to comprehensively study timely responses in wireless communication for post-earthquake recovery [20]. Moreover, there is uncertainty in the availability of the network [21], and a realistic post-earthquake network model is currently lacking in the literature. A large-scale disaster may affect an area with a certain or probabilistic shape, which can be used to create a more realistic post-earthquake network model [11]. However, this requires a multidisciplinary study encompassing civil/structural engineering and wireless engineering.

The study of disaster modeling from a seismic perspective has emerged as a critical field of research, driven by the need to better understand and mitigate the devastating impact of earthquakes on communities and infrastructure. Multiple property damage estimation models for building collapse, road blockage, and fire spread, have been developed in [22] to create a city-damage simulation model using data from observations following the striking earthquakes. In [23], the authors introduce an integrated approach for probabilistic systemic risk analysis of a road network taking into account spatial seismic hazard, correlations in ground motion intensities, and the vulnerability of network components. Additionally, the work in [24] presents a method to assess the seismic performance of large-scale electric power systems under spatially correlated earthquake ground motions utilizing network flow theory for power flow allocation. A three-step framework for assessing vulnerability due to earthquake-like hazards is proposed in [25], accounting for creating an inventory of road networks, conducting vulnerability assessments of building structures, and analyzing the impact of road closures to assist emergency managers in pinpointing vulnerable sections of the road network and implementing essential mitigative actions. A pioneering method is introduced in [26] to assess the functionality of city building portfolios after an earthquake, whose findings can contribute to forecasting the likelihood of functional losses before earthquakes, steering the post-earthquake recovery process, and implementing proactive measures to enhance the seismic resilience of cities.

The post-earthquake city model accurately represents the damage and destruction incurred by the disaster, including the collapsed buildings and disrupted infrastructure for insightful estimation of inoperable rooftop BSs and road blockages, respectively. The routing of MDRUs in an earthquake aftermath, becomes a critical aspect of establishing quick and effective communication infrastructure to cover gaps or holes in network coverage [27]. Through careful planning and analysis, their routing should be efficient, ensuring that they are located in a way that maximizes coverage and minimizes signal interference or obstruction caused by debris or damaged infrastructure.

A. RELATED WORKS

In the realm of post-disaster communication, a striking gap in the literature becomes evident when considering seismic-related properties. The majority of works in this field tend to generalize the requirements and specifications for post-disaster wireless networks, neglecting the specific seismic factors that can disrupt or damage infrastructure. In fact, only a handful of works have utilized seismic factors for post-earthquake communication restoration. The research in [28] explores how seismic ground motion models can be used to simulate the effects of earthquakes on smart grid communication networks. A methodology to model and quantify the seismic vulnerability and resilience of communication is studied in [29], where the network infrastructure's physical dependence on the underlying building was considered. The vulnerability of Venezuela's state communications network to earthquakes was examined in [30]. This investigation for failures of network nodes was evaluated using probabilistic risk analysis methods, incorporating historical seismic data and Monte Carlo simulations. Nodes and arcs were concurrently evaluated, following the methodology outlined in [31]. This approach employed probabilistic seismic hazard analysis to predict the condition of network elements post-earthquake. The methodology integrates a seismic source model and ground prediction equations to assess the intensity measurement of each component relative to its location. During simulation, node failures align with building fragility curves, while a failure rate contingent upon the current rating and cable attributes determines link failures. Recently, in [32], a regional seismic risk assessment framework was developed to quantify the vulnerability of post-earthquake functionality of small, macro BSs, and combined heterogeneous structure under earthquake hazard threats, particularly in the context of 5G.

B. MOTIVATION AND CONTRIBUTIONS

A comprehensive probabilistic model of earthquake excitation, encompassing ground motion intensity distribution, fragility functions, building collapse probability, debris width calculation, and road open section probability, has yet to be modeled and their impacts on the communication infrastructure need to be analyzed. This is crucial given the inherent interdependence between cellular networks and earthquake events. Our research addresses this gap by focusing on rooftop BSs failure and building collapse within a Manhattan grid-based city architecture.[1] In addition to developing a realistic network model for post-earthquake communication, we are taking a further step by providing insights applicable to urban emergency response strategies. This involves considering the communication recovery aspect, specifically deploying recovery units within survivor cellular communication networks. Our work extends further to propose a routing algorithm for first responders, facilitating access to damaged BSs or MDRUs at desired locations amidst collapsed buildings and closed roads caused by the post-earthquake city model. Lastly, we are conducting the proof of the seismic model equation's reliability and assessing the network model's performance under varying seismic parameters, emphasizing its practical implications for emergency management. Also, the effectiveness of the proposed routing algorithm in managing road closures is evaluated. Briefly, we study the following contributions:

- Defining a probabilistic model for cellular network coverage in a post-earthquake scenario, considering BS collapse and road blockage.
- Proposing a routing algorithm for first responders to reach the damaged BSs or MDRUs at desired locations in a post-earthquake scenario involving collapsed buildings and closed roads.
- Conducting extensive simulations to evaluate the performance of the network model under various seismic parameters and assess the effectiveness of the proposed routing algorithm in managing road closures.

C. PAPER NOTATIONS AND ORGANIZATIONS

Notations: Throughout the paper, the i, n, and j denote the BS_i, MDRU_n, and user equipment $(\text{UE})_j$ respectively. The $\mathcal{LN}(a, b)$ notates a log-normal random variable with mean a and standard deviation of b. The conditional probability is given as $P(A|B)$ that calculates the probability of an event A given that another event B has occurred. The $\Phi()$ is the standard normal cumulative distribution function (CDF). The $\overset{(a)}{=}$ and the $\overset{(a)}{\approx}$ represent the transition and approximation in (a), respectively. The notation B' stands for the building located opposite B. $|.|$ represents the number of components. w_a^b denotes the weight between a and b vertices in the graph. $\lfloor . \rfloor$ and $a \bmod b$ represent floor and the modulo operations, respectively, where $c \equiv a \bmod b$.

Organization: The rest of this paper is organized as follows. Section II describes the general city and network system models with performance metrics. The probabilistic model of earthquake excitation is explained with mathematical analyses in Section III. The proposed routing algorithm and deployment of MDRUs for post-earthquake scenario is included in Section IV. The numerical simulation results and analysis are given in Section V. Finally, Section VI provides a conclusion.

[1]The Manhattan-city layout is chosen without loss of generality and for simplicity of exposition.

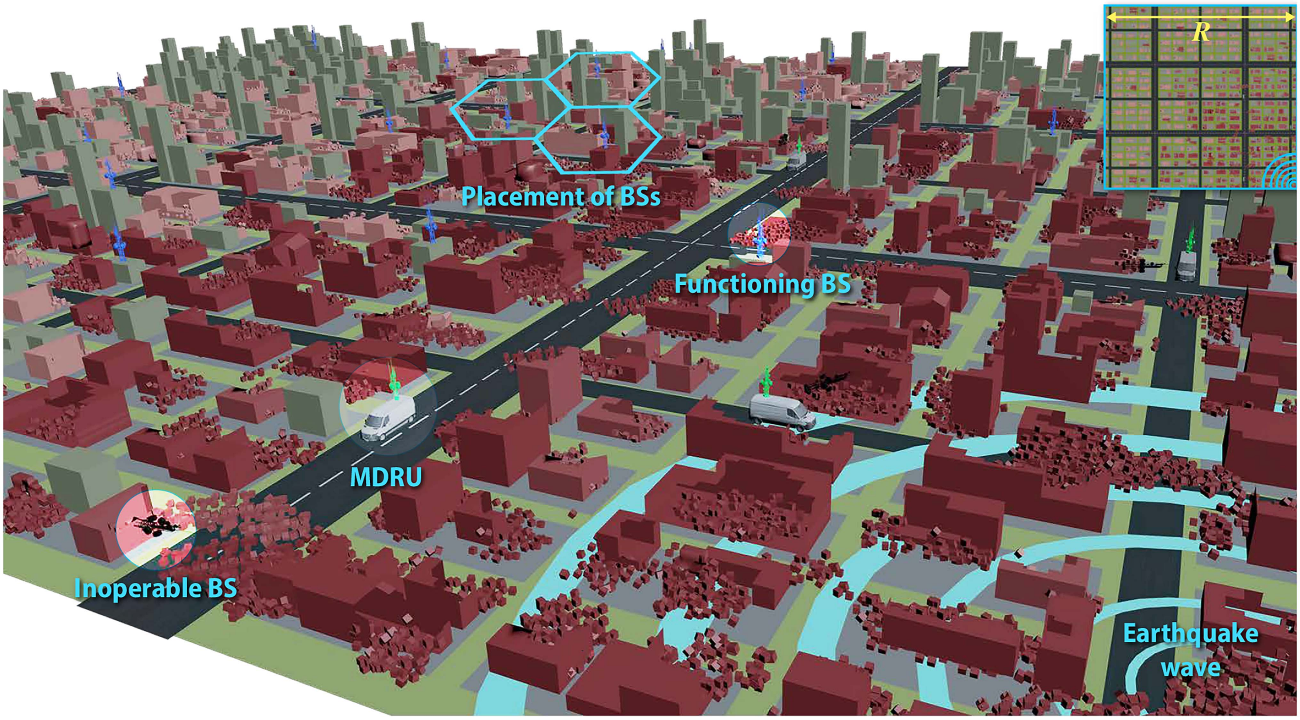

FIGURE 1. The geographical layout of the post-earthquake Manhattan grid-based city model and heterogeneous network model with MDRUs. The redness on the buildings indicates the extent of damage caused by the earthquake.

II. SYSTEM MODEL

In this work, we consider a Manhattan-grid-based city model, where the city is divided into identical square-shaped regions of length R, by identical streets featuring R_{R} width, and Q R_{R}-wide identical avenues, where $Q > 1$. The city buildings are assumed to have identical square footprints of R_{B} side length and are uniformly distributed amongst the city square regions as depicted in Fig. 1, where each road accommodates R_{S} buildings, and avenues are regularly placed with R_{Q} roads-separation intervals along both the X and Y axes. As for the buildings' heights, they are assumed to follow a Rayleigh distribution parameterized by γ as outlined in the universal statistical model for building deployment provided by ITU-R Rec. P1410 [33], where γ denotes the most common building height.

As described in the 3GPP Manhattan deployment scenario [34], we adopt a hexagonal cellular network layout where macro BSs are deployed on buildings' rooftops, with cell radius R_{M} with a unity frequency re-use factor. Furthermore, the BSs are considered to transmit at P_{T} power to serve its associated UEs. In this work, users are associated with BSs based on the strongest received signal strength (RSS). Moreover, all the intra-cell communication links operate in an orthogonal fashion, i.e., interfering sources are always from neighboring cells. After an earthquake hits, we assume that BSs destruction is associated with their building collapse. In addition, we assume that the number of deployed MDRUs to restore network coverage, matches the number of collapsed BSs. Fig. 2 represents the main components of the city and network model, where we assume that all the MDRUs are identical with P_{V}, V_{h}, and V_{d} representing the MDRUs' transmit power, antenna height, and vehicle width, respectively.

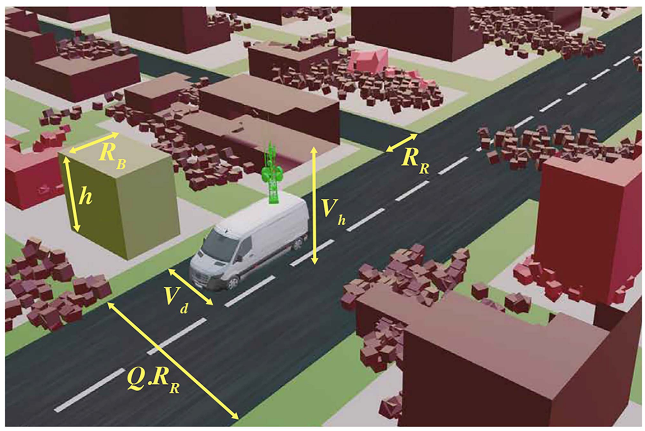

FIGURE 2. The main components of the city and network model.

Given that UE_j is associated with BS_i, the communication channel imperfections are assumed to be dominated by large-scale fading, where the received power for the UE_j is expressed as

$$P_{\mathrm{rx}}^{i,j} = P_{\mathrm{T}}\left(R_{\mathrm{U}}^{i,j}\right)^{-\eta}\alpha^{i,j}, \tag{1}$$

where $R_{\mathrm{U}}^{i,j}$ is the distance between the BS_i and UE_j; η is the path loss exponent; $\alpha^{i,j} = 10^{\zeta^{i,j}/10}$ represents the log-normal shadowing; and $\zeta^{i,j}$ is a normally distributed random variable with zero mean and standard deviation σ_S. With similar derivation of $P_{rx}^{i,j}$ in (1), where $i' \neq i$, the interference power introduced by $BS_{i'}$ on UE_j would be

$$P_{int}^{i',j} = P_T \left(R_U^{i',j}\right)^{-\eta} \alpha^{i',j}, \quad (2)$$

where $R_U^{i',j}$ and $\alpha^{i',j}$ represent the distance and the shadowing between UE_j and $BS_{i'}$, respectively. Accordingly, the signal-to-interference-plus-noise-ratio (SINR) of UE_j in a network with a total of K BS, including terrestrial BSs and MDRUs, can be expressed as follows:

$$\psi^{i,j} = \frac{P_T \left(R_U^{i,j}\right)^{-\eta} \alpha^{i,j}}{\sum_{\substack{k=1 \\ k \neq i}}^{K-1} P_T \left(R_U^{k,j}\right)^{-\eta} \alpha^{k,j} + \sigma_j^2}, \quad (3)$$

where $\sigma_i^2 = N_0 B$ is the thermal noise power at UE_j's receiver, N_0 is the noise power spectral density, $B = BW/U^i$ is the bandwidth allocated to UE_j, BW is the total bandwidth available for BS_i, and U^i is the total number of UE associated with BS_i.

Outage probability and capacity are also used as performance metrics to assess restoration of the cellular network through optimal deployment of MDRUs while ensuring that the distance between radio units is maximized to minimize interference. Following from (3), the outage probability for UE_j is expressed as

$$P_{out}^{i,j} = \mathcal{P}\left(\psi^{i,j} < \psi^{th}\right), \quad (4)$$

where ψ^{th} is the threshold value characterizing the desired SINRs for UEs. The capacity is defined as the upper bound on the information rate that can be communicated through a channel subject to the additive white Gaussian noise (AWGN), and it can be calculated as $C^{i,j} = B \log_2(1 + \psi^{i,j})$.

III. POST-EARTHQUAKE INFRASTRUCTURE MODEL

In this section, we propose a stochastic model that describes the infrastructure damage after an earthquake, which will be exploited in Section IV to propose an efficient algorithm for network coverage restoration. In the following subsections, we illustrate in detail the whole destruction process starting with the earthquake excitation and the associated randomness of ground motion. Next, we elaborate on the correlation between ground motion severity and the likelihood of building collapse. Finally, we characterize the generated debris due to infrastructure destruction and the potential road blockage impacts.

The important assumptions in our post-earthquake model are as follows:

- The peak ground acceleration (PGA) is assumed to follow a log-normal distribution, capturing variability in ground motion.
- The probability distribution at each point for PGA is distance-dependent. However, PGA values at different locations are modeled as independent, without accounting for spatial correlation.
- The building heights are modeled with a Rayleigh distribution, assuming independence in height between buildings at different locations.
- Building collapse event is modeled as conditionally independent given the local PGA value, with no correlation in material or structural factors between buildings.
- Empirically derived fragility curves estimate collapse probability based on PGA, without accounting for construction-specific dependencies (e.g., age).
- Identical Buildings' horizontal footprint and horizontal alignment of buildings overlooking the same street.

As long as the provided assumptions are met, the proposed model can be applicable to any city layouts. The fundamental input random variables, dependencies across the variables, and how randomness is structured within the proposed seismic model for city destruction are visualized as a computational graph in Fig. 3.

A. EARTHQUAKE AS A STOCHASTIC PROCESS

In seismic hazard analysis literature, there is a multitude of methods to model earthquakes that mostly fall within two main categories: analytical models and empirical models [35]. In analytical models, an earthquake is considered a seismic wave formulated by using differential equations with boundary conditions dictated by the scenario-specific circumstances. Despite the offered accuracy of such models, they are computationally very expensive and might not be practical to be employed by first responders. On the other hand, empirical ground motion models focus on providing a statistical description of the main dynamic features of the earthquake, such as the peak ground acceleration (PGA), peak ground velocity (PGV), and spectral acceleration (SA). In this work, we focus on empirical models for PGA, as they are widely adopted in probabilistic hazard assessment analysis, and their associated relatively low-computational complexity costs lend themselves to a limited time needed to respond to the catastrophe.

1) GROUND MOTION INTENSITY DISTRIBUTION

An empirical ground motion model, which predicts the ground motion intensity typically takes the following general probabilistic form:

$$\mathcal{IM} \sim \mathcal{LN}\left(\mu_{lnIM}, \sigma_{lnIM}^2\right), \quad (5)$$

where intensity measure (IM) is the ground motion parameter of interest such as PGA or SA, being a log-normal random variable with mean μ_{lnIM} and standard deviation of σ_{lnIM} [35]. In our earthquake modeling, the updated version of the CY14 model is adopted based on analysis of the ground motion data from the significantly expanded NGA-West2 dataset [36]. This study adapts PGA as a widely recognized measure of ground motion intensity to assess the potential impact of an earthquake on buildings' structures. Based on (5), PGA is a random variable described by a

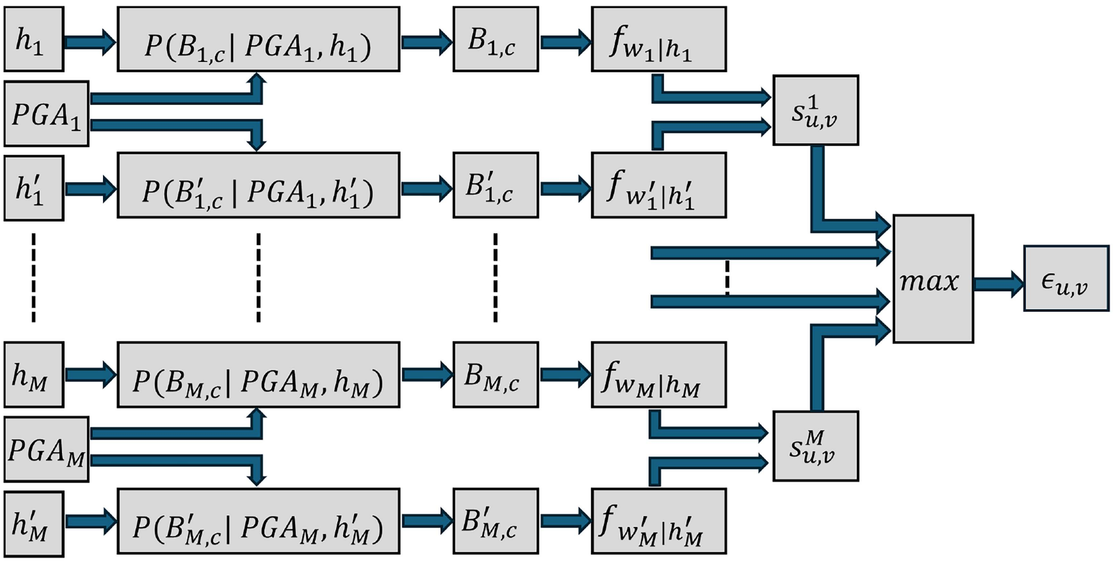

FIGURE 3. Fundamental input random variables and computational graph used in the seismic model for city destruction.

log-normal distribution. Following the same notation in [36], the logarithmic mean of PGA for a given T can be written as [36, (eq. 11)]

$$\mu_{lnPGA} = f\left(\chi, M_q, R_{ss}, V_{s30}, Z_{10}, \delta, \vec{\theta}|T\right), \tag{6}$$

where f is a tedious function of earthquake parameters; χ is the location of the earthquake epicenter; M_q is the earthquake moment magnitude; R_{ss} is the source-to-site distance; V_{S30} is the 30-meter time-averaged shear-wave velocity; Z_{10} is the depth from the ground surface to the 1 km/s shear-wave horizon; δ is fault dip angle (in °); and $\vec{\theta}$ are the regression coefficients depending on parameter T, which typically represents the period of vibration or oscillation of the ground motions. We would like to note that the mean value of PGA is predominantly influenced by the earthquake magnitude and the distance from the earthquake source. Higher earthquake magnitudes generally lead to higher mean values, indicating stronger ground shaking. Conversely, greater distances from the earthquake source usually result in lower mean values due to wave attenuation and geometric spreading. Soil type can also affect the mean of PGA, with softer soils and irregular topographies generally leading to higher values. On the other hand, total variance is given by [36, (eq. 13)]

$$\sigma_T^2 = g\left(\tau, NL_0, \sigma_{NL_0}\right) \tag{7}$$

where g is a complex function of ground motion parameters; τ is the between-earthquake residual variance; NL_0 term measures the non-linearity in site response and σ_{NL_0} is the standard deviation of non-linearity in site response. The standard deviation of the PGA reflects the variability in ground motion prediction. It is affected by earthquake magnitude, distance from the source of the earthquake, and local site conditions. Smaller magnitudes and shorter distances generally lead to higher variability. Soil type and site-specific effects also affect the standard deviation. Further details on the model and corresponding parameters can be found in [36].

2) FRAGILITY FUNCTIONS AND PROBABILITY OF COLLAPSE

Given, the previously defined ground motion model, the next step towards the statistical model of destruction is to evaluate the buildings' collapse probability. The pivotal element in this process is the building fragility curve a.k.a fragility function. Fragility refers to the likelihood that a structure will reach damage at a certain level when subjected to a specific earthquake intensity. The fragility function of a certain structure is the conditional probability of the structure collapse given a certain ground motion level. The fragility function is assumed to have a log-normal behavior, given as

$$F_R(x) = \mathcal{P}(C|PGA = x) = \Phi\left(\frac{ln(x) - \mu}{\beta}\right) \tag{8}$$

where $\mathcal{P}(C|PGA = x)$ is the probability that the building will collapse under a ground motion with IM being $PGA = x$, $\Phi(\cdot)$ is the standard normal CDF, μ and β standing for the mean and standard deviation, respectively, are constants that depend on the building characteristics as structure, cross-section area, and height, to name a few [37]. These constants are crucial as they account for the variability in building responses to seismic events and provide a measure of the building's resilience. In this work we adopt the models proposed in [38] for μ and β as functions of the building height (h) which could be utilized for every class of buildings: reinforced concrete (RC), steel or masonry buildings. Particularly,

$$\mu(h) = 5 * 10^{-5} * h^2 - 0.0023 * h - 0.0666, \tag{9}$$
$$\beta(h) = 6 * 10^{-4} * h^2 - 0.0283 * h + 0.4708. \tag{10}$$

The building collapse probability depends on both earthquake characteristics and building structure, particularly

PGA and building height, respectively. By averaging out the uncertainty in the building fragility function represented in the PGA measured at the building location and height, the building probability of collapse is expressed as

$$\mathcal{P}_C = \int_0^\infty \int_0^\infty F_R(PGA) f_H(h) f_{PGA}(x) dh dx$$
$$= \int_0^\infty \int_0^\infty \Phi\left(\frac{ln(x) - \mu(h)}{\beta(h)}\right) \frac{h}{\gamma^2} \exp\left(-\frac{h^2}{2\gamma^2}\right)$$
$$\times \frac{1}{x\sqrt{2\pi}\sigma_{lnPGA}} \exp\left(-\frac{1}{2}\left(\frac{ln(x) - \mu_{lnPGA}}{\sigma_{lnPGA}}\right)^2\right) dh dx, \tag{11}$$

where $f_H(h)$ is the Rayleigh distribution of building's height and $f_{PGA}(x)$ is the PGA probability density function (PDF). This formulation incorporates the uncertainty in both the structural characteristics and the seismic hazard, leading to a more robust estimation of the building collapse probability under varying conditions.

The probability of building collapse plays a critical role in our proposed probabilistic city model, as it influences both base station BS collapses and road closures. MDRUs are designed to provide temporary coverage by positioning themselves near collapsed BS sites. Therefore, understanding the probability of BS collapse and the likelihood of road closures due to building failures is essential for strategic MDRU deployment. This ensures that communication coverage can be restored as close as possible to pre-disaster levels.

3) ROAD BLOCKAGE

Now, having quantified the probability of building collapse, which also defines the probability of BSs destruction, it remains to quantify the likelihood of having a neighboring road getting blocked by the collapsed building debris. towardss this aim, we adopt the geometric building debris model [39], where debris is assumed to fall uniformly from a collapsed building, and conditional PDF for the debris width ω is given by the following triangular distribution as

$$f(\omega|h) = \begin{cases} \frac{2(\omega-a)}{(b-a)(c-a)} & a \leq \omega \leq c \\ \frac{2(b-\omega)}{(b-c)(b-a)} & c < \omega \leq b \end{cases} \tag{12}$$

where $f(\omega|h)$ is the conditional probability distribution of the debris width given a certain height, a is the minimum, b is the maximum, c is the mode, specified as $h/8$, $h/2$ and $h/4$, respectively [39]. Based on the conditional PDF for debris width, the unconditioned PDF that assimilates the Rayleigh height PDF is provided by the following Lemma.

Lemma 1: The PDF of debris width generated by building collapse for a city with Rayleigh distributed building heights with parameter γ is given by

$$f_\Omega(\omega) = \frac{8}{3\gamma^2}\omega \sum_{p=0}^{2} a_p \mathrm{ei}\left(\frac{(-2)^{2p+1}}{\gamma^2}\omega^2\right)$$
$$+ \frac{8\sqrt{2\pi}}{3\gamma} \sum_{q=0}^{2} b_q \mathrm{erf}\left(\frac{2^q\sqrt{2}}{\gamma^2}\omega\right), \tag{13}$$

where ei(.) is the exponential integral, erf(.) is the error function expressed as $\mathrm{ei}(z) = \int_z^\infty \frac{\exp(-t)}{t} dt$ and $\mathrm{erf}(z) = \frac{2}{\sqrt{\pi}} \int_0^z \exp(-t^2) dt$, respectively.

Proof: Please see Appendix 1. ■

This brings us one step closer towardss finding the road section blockage probability, which is determined by the contributions of the overlooking collapsed buildings' debris. A road segment is considered closed if any of its sections is closed. The blockage status of the road segment between the road intersections υ and ν, is represented by a Bernoulli random variable $\epsilon_{\upsilon,\nu} \in \{0, 1\}$, where $\epsilon_{\upsilon,\nu} = 1$ denotes the road section closure. A road section is open, when the overall debris of the two buildings overlooking the road section is not large enough to block vehicles passage. Specifically, for a given segment $\epsilon_{\upsilon,\nu}$, $s^m_{\upsilon,\nu} = 0$ indicates that its m-th road section is open, allowing vehicles to pass through without hindrance, equivalently, $w_m + w'_m \leq S_\mathrm{W} - V_\mathrm{W}$, where w_m, w'_m are the debris widths of B and B', respectively, S_W and V_W are the street and vehicle widths, respectively. Similarly, the $m-$th section closure status of the $\epsilon_{\upsilon,\nu}$ is represented by another Bernoulli variable $s^m_{\upsilon,\nu}$, with $s^m_{\upsilon,\nu} = 1$ denoting the blockage of the $m-$th section of the $\epsilon_{\upsilon,\nu}$. Accordingly, the probability of closure for $\epsilon_{\upsilon,\nu}$ is expressed as

$$\mathcal{P}\big(\epsilon_{\upsilon,\nu} = 1\big) = 1 - \mathcal{P}\big(\epsilon_{\upsilon,\nu} = 0\big) \tag{14}$$
$$= 1 - \mathcal{P}\left(\bigcap_{m=1}^{M} s^m_{\upsilon,\nu} = 0\right) \tag{15}$$
$$\overset{(a)}{=} 1 - \prod_{m=1}^{M} \mathcal{P}\big(s^m_{\upsilon,\nu} = 0\big) \tag{16}$$
$$\overset{(b)}{\approx} 1 - \mathcal{P}\big(s^m_{\upsilon,\nu} = 0\big)^M, \tag{17}$$

where M is the number of road sections within a road segment. The transition in (a) follows from the independence of section blockage events due to the independence of buildings' heights. The approximation followed in transition (b) stems from the high similarity in section closure probabilities that belong to the same road segment as the distances between the included buildings and the earthquake epicenter are very similar.Finally, the probability of having section $s^m_{\upsilon,\nu}$ open, is mathematically expressed by using the law of total probability as

$$\mathcal{P}\big(s^m_{\upsilon,\nu} = 0\big) = \mathcal{P}\big(s^m_{\upsilon,\nu} = 0|B_\mathrm{C}, B'_\mathrm{C}\big)\mathcal{P}(B_\mathrm{C})\mathcal{P}\big(B'_\mathrm{C}\big)$$
$$+ \mathcal{P}\Big(s^m_{\upsilon,\nu} = 0|B_C, B'_{\bar{\mathrm{C}}}\Big)\mathcal{P}(B_C)\mathcal{P}\Big(B'_{\bar{\mathrm{C}}}\Big)$$
$$+ \mathcal{P}\big(s^m_{\upsilon,\nu} = 0|B_{\bar{\mathrm{C}}}, B'_\mathrm{C}\big)\mathcal{P}(B_{\bar{\mathrm{C}}})\mathcal{P}\big(B'_\mathrm{C}\big)$$
$$+ \mathcal{P}\Big(s^m_{\upsilon,\nu} = 0|B_{\bar{\mathrm{C}}}, B'_{\bar{\mathrm{C}}}\Big)\mathcal{P}\big(B_{\bar{\mathrm{C}}}\big)\mathcal{P}\Big(B'_{\bar{\mathrm{C}}}\Big), \tag{18}$$

where $\mathcal{P}(B_\mathrm{C})$ and $\mathcal{P}(B'_\mathrm{C})$ are the probability of collapse of building B and its opposite B', respectively, while $\mathcal{P}(B_{\bar{\mathrm{C}}}) = 1-\mathcal{P}(B_\mathrm{C})$ and $\mathcal{P}(B'_{\bar{\mathrm{C}}}) = 1-\mathcal{P}(B'_\mathrm{C})$. Basically, (18) calculates the probability that a section is open by considering all possible combinations of the collapse or non-collapse of every two buildings within the same road section, B and B'.

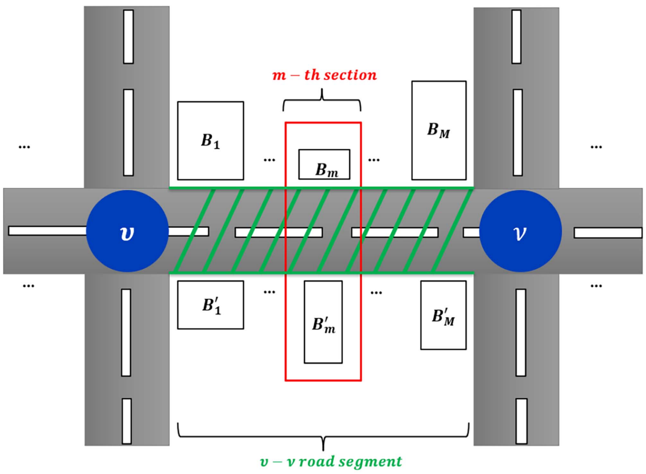

FIGURE 4. Section composition of a road segment.

The equation sums four terms, each of which represents a different combination of the section's buildings collapse status where $(B_{\mathrm{C}}, B'_{\mathrm{C}})$, $(B_{\mathrm{C}}, B'_{\bar{\mathrm{C}}})$, $(B_{\bar{\mathrm{C}}}, B'_{\mathrm{C}})$, $(B_{\bar{\mathrm{C}}}, B'_{\bar{\mathrm{C}}})$ indicate both buildings collapsed, only B collapsed, only B' collapsed, and neither building collapsed, respectively. Each term is the product of the conditional probability that a $s^m_{\upsilon,\nu}$ section is open given the specific collapse scenario, multiplied by the individual probabilities of that scenario occurring, i.e., $\mathcal{P}(B_{\mathrm{C}})$ for B collapsing and its complement $\mathcal{P}(B_{\bar{\mathrm{C}}})$ or $\mathcal{P}(B'_{\mathrm{C}})$ for B' collapsing and its complement $\mathcal{P}(B'_{\bar{\mathrm{C}}})$. A simple illustration of the section composition of a road segment with the associated buildings, B_m and its opposite B'_m for $m = 1, 2, \ldots, M$, is shown in Fig. 4. In this work, $\mathcal{P}(s^m_{\upsilon,\nu} = 0|B_{\bar{\mathrm{C}}}, B'_{\bar{\mathrm{C}}}) = 1$, as we are not considering the road cracks caused by the earthquake.

Lemma 2: For the considered Manhattan-grid city model and Rayleigh buildings' heights distribution with parameter γ, the open road section probability given the two overlooking buildings collapsed is given as

$$
\begin{aligned}
&\mathcal{P}\left(s^m_{\upsilon,\nu} = 0|B_{\mathrm{C}}, B'_{\mathrm{C}}\right) \\
&= \int_0^{d_{\mathrm{th}}} f_{\Omega}(\omega')\Bigg(\frac{1}{3}\sum_{i=0}^{2} c_i \exp\left(\frac{(-2)^{2i+1}}{\gamma^2} d'_{\mathrm{th}}\right) \\
&\quad + \frac{\sqrt{2\pi}}{3\gamma} d_{\mathrm{th}} \sum_{j=0}^{2} c_j \mathrm{erf}\left(\frac{2^j\sqrt{2}}{\gamma} d'_{\mathrm{th}}\right) \\
&\quad + \frac{1}{3\gamma^2} d_{\mathrm{th}}^2 \sum_{k=0}^{2} c_k \Gamma\left(0, \frac{2^{2k+1}}{\gamma^2} d'^2_{\mathrm{th}}\right) \\
&\quad - \frac{8}{3\gamma^2}\omega'\Bigg(\sqrt{2\pi}\gamma \sum_{l=0}^{2} c_l \mathrm{erf}\left(\frac{2^l\sqrt{2}}{\gamma} d'_{\mathrm{th}}\right) \\
&\quad + \frac{1}{3\gamma^2} d_{\mathrm{th}} \sum_{m=0}^{2} c_m \Gamma\left(0, \frac{2^{2m+1}}{\gamma^2} d'^2_{\mathrm{th}}\right)\Bigg) \\
&\quad + \frac{16}{3\gamma^2}\omega'^2 \sum_{n=0}^{2} c_n \Gamma\left(0, \frac{2^{2n+1}}{\gamma^2} d'^2_{\mathrm{th}}\right) - 1\Bigg) d\omega', \qquad (19)
\end{aligned}
$$

and the corresponding probability given a single overlooking building collapsed is

$$
\begin{aligned}
&\mathcal{P}\left(s^m_{\upsilon,\nu} = 0|B_{\mathrm{C}}, B'_{\bar{\mathrm{C}}}\right) \\
&= \frac{1}{3}\sum_{u=0}^{2} c_u \exp\left(\frac{(-2)^{2u+1}}{\gamma^2} d_{\mathrm{th}}^2 - 1\right) \\
&\quad + \frac{1}{3}\gamma \sum_{v=0}^{2} c_v \exp\left(\frac{(-2)^{2v+1}}{\gamma^4} d_{\mathrm{th}}^2 - 1\right) \\
&\quad + \frac{\sqrt{2\pi}}{3\gamma} d_{\mathrm{th}} \sum_{y=0}^{2} c_y \mathrm{erf}\left(\frac{2^y\sqrt{2}}{\gamma^2} d_{\mathrm{th}}\right) \\
&\quad + \frac{2}{3\gamma^2} d_{\mathrm{th}}^2 \sum_{z=0}^{2} c_z \Gamma\left(0, \frac{2^{2z+1}}{\gamma^2}\right). \qquad (20)
\end{aligned}
$$

Proof: Please see Appendix B. ■

By substituting (19) and (20) into (18), we obtain the probability of having an open $s^m_{\upsilon,\nu}$ section. Subsequently, substituting (18) into (17) allows us to complete the evaluation of the probability of the road segment $\epsilon_{\upsilon,\nu}$ being closed.

In summary, incorporating uncertainty and correlation is crucial for understanding the potential impacts on network restoration. As given in Fig. 3, obtaining fragility curves (8) is an inevitable key step in seismic risk assessment in performance-based earthquake engineering which accounts for the uncertainties of risk due to seismic events. The probabilities calculated for building collapse (11), debris width (12), and subsequent road blockage (14) inform our algorithm for restoring network coverage, emphasizing the importance of these factors in strategic decision-making, particularly for first responders.

IV. LOW-COMPLEXITY MDRUS ROUTING SOLUTION TO RESTORE NETWORK COVERAGE

In this section, we address the routing problem of the MDRUs aiming to restore communications coverage performance as close as possible to the pre-disaster levels by strategically deploying MDRUs to their best locations in the least possible time. For simplicity, let's assume that the operator has a sufficient number of MDRUs to compensate for the $N \leq K$ collapsed BSs, whose set is denoted by $\mathcal{N}$. Accordingly, each of the MDRUs is targeted to reach as close as possible to collapsed BS sites and provide temporary coverage. The absence of prior knowledge about collapsed roads implies that following the shortest path to the destination does not guarantee optimal travel times. Consequently, we will leverage road closure likelihoods derived in the previous section to come up with a probabilistic routing solution.

Let us consider a Manhattan-grid-based city road network with the number of horizontal and vertical roads are represented as E_{h} and E_{v}, respectively. The mathematical

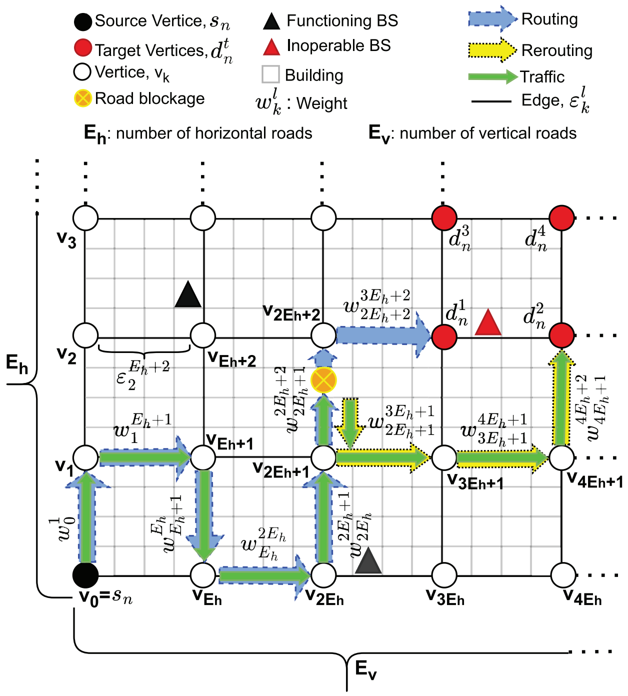

FIGURE 5. Road network graph and routing illustration.

description of E_h and E_v for the R length square-shaped region can be expressed as

$$E_\mathrm{h} = E_\mathrm{v} = R_\mathrm{Q}\left\lfloor \frac{R}{\mathrm{A}} \right\rfloor + \left\lfloor \frac{R \bmod \mathrm{A}}{\mathrm{S}} \right\rfloor, \tag{21}$$

where $\mathrm{S} = \mathrm{R_B R_S} + \mathrm{R_R}$ and $\mathrm{A} = \mathrm{R_Q S} + \mathrm{R_R}(\mathrm{Q}-1)$ are defined as the unique distance between two parallel road segments and avenues, respectively. Fig. 5 illustrates a Manhattan-grid based city model for $R_\mathrm{S} = 4$, $E_\mathrm{h} = 4$, and $E_\mathrm{v} = 5$. Such a road network can be modeled as a bi-directed graph denoted by $\mathcal{G} = (\mathcal{V}, \mathcal{E}, \mathcal{W})$, where $V = E_\mathrm{h} \times E_\mathrm{v}$ road intersections is represented by the vertex set $\mathcal{V} = \{v_k | k \in [1, V]\}$; $\mathcal{E} = \{\varepsilon_k^l | k, l \in \mathcal{V},\ k \neq l\}$ represents $|\mathcal{E}| = E = (E_\mathrm{h} - 1) \times (E_\mathrm{v} - 1)$ road segments; and $\mathcal{W} = \{w_k^l | k, l \in \mathcal{V},\ k \neq l\}$ is the set of non-negative edge weights, $w_k^l \in \mathbb{R}^+$, which are directly associated with corresponding road segments, ε_k^l, $\forall k, \forall l$, i.e., $|\mathcal{W}| = W = E$. We denote the ordered set of 4 vertices nearest to the n^{th} collapsed BS by $\mathcal{T}_n, n \in \mathcal{N}$, which is sorted in ascending order of Euclidean distance to the n^{th} collapsed BS. In order to increase the chance of finding a feasible route to the n^{th} collapsed BS, MDRU$_n$ sequentially takes vertices within $\mathcal{T}_n$ as its destination starting from the closest member. If we denote the source vertex as s_n and t^{th} closest vertex as d_n^t, where $d_n^t \in \mathcal{T}_n$ and $t \in [1, 4]$, $s_n \rightsquigarrow d_n^t = \{s_n, \ldots, d_n^t\} \in \mathcal{R}_n^t$ defines any arbitrary route from s_n to d_n^t as an ordered sequence of vertices MDRU$_n$ visits during its journey, where $\mathcal{R}_n^t$ is a superset of all R_n^t possible routes for MDRU$_n$. Accordingly, the success probability of MDRU$_n$ over the r^{th}, $r \in [1, R_n^t]$, arbitrary route is given by

$$\mathcal{P}_{n,t}^r = \prod_{\substack{\forall k, l \in \mathcal{R}_n^t\{r\} \\ k \neq l}} w_k^l, \tag{22}$$

where w_k^l is defined as the probability of an open road between vertices k and l and follows from Lemma 2. Accordingly, the routing problem of interest for MDRU$_n$ can be expressed as

$$s_n \rightarrowtail d_n^t = \mathcal{R}_n^t \left\{ \underset{\forall r \in \mathcal{R}_n^t}{\arg\max} \left\{ \mathcal{P}_{n,t}^r \right\} \right\}, \tag{23}$$

where $s_n \rightarrowtail d_n^t$ is the optimal path from s_n to d_n^t with the highest probability of success.

Even though shortest path algorithms (SPAs) are a common choice to find the best route, their additive nature and cumulative distance approach can not be applied to solve (23) for finding the path with the highest probability of success. In order to leverage SPAs, we perform the following transformation on (23) to obtain an equivalent problem

$$\begin{aligned} s_n \rightarrowtail d_n^t &\overset{(a)}{=} \mathcal{R}_n^t \left\{ \underset{\forall r \in \mathcal{R}_n^t}{\arg\max} \left\{ \log\left(\prod_{\substack{\forall k, l \in \mathcal{R}_n^t\{r\} \\ k \neq l}} w_k^l \right) \right\} \right\} \\ &\overset{(b)}{=} \mathcal{R}_n^t \left\{ \underset{\forall r \in \mathcal{R}_n^t}{\arg\max} \left\{ \sum_{\substack{\forall k, l \in \mathcal{R}_n^t\{r\} \\ k \neq l}} \log\left(w_k^l\right) \right\} \right\} \\ &\overset{(c)}{=} \mathcal{R}_n^t \left\{ \underset{\forall r \in \mathcal{R}_n^t}{\arg\min} \left\{ - \sum_{\substack{\forall k, l \in \mathcal{R}_n^t\{r\} \\ k \neq l}} \log\left(w_k^l\right) \right\} \right\}, \\ &\overset{(d)}{=} \mathcal{R}_n^t \left\{ \underset{\forall r \in \mathcal{R}_n^t}{\arg\min} \left\{ \sum_{\substack{\forall k, l \in \mathcal{R}_n^t\{r\} \\ k \neq l}} \tilde{w}_k^l \right\} \right\}, \end{aligned} \tag{24}$$

where (a) holds due to the monotonically increasing nature of logarithmic functions, (b) follows from the product rule of the logarithm, (c) transforms the resulting maximization problem into a minimization one through negation; and (d) provides an equivalent problem that allows utilizing SPAs on a revised graph $\widetilde{\mathcal{G}} = (\mathcal{V}, \mathcal{E}, \widetilde{\mathcal{W}})$ with modified edge weights, i.e., $\widetilde{w}_\upsilon^\nu = \log(1 - \mathcal{P}(\epsilon_{\upsilon,\nu} = 1))$. The optimization problem in (24) gives output between 0 to ∞ for successful and failed routing, respectively.

It is worth noting that the best route obtained from the probabilistic approach developed in (24) only provides the highest success probability of reaching d_n^t from s_n; however, reaching the final destination is not guaranteed in real life as the actual road status between vertices k and l, $\epsilon_k^l \in \{0, 1\}$, follows a Bernoulli distribution as explained in the previous section. In other words, it is possible for MDRU$_n$ to encounter a dead end even if it follows the best route provided by the SPA as illustrated in Fig. 5. Therefore, we consider an adaptive and cooperative framework as follows: when MDRU$_n$ encounters a road closure in real life, it reruns SPA to find the best route from the last successfully visited vertex and broadcasts the edge weight updates on $\widetilde{\mathcal{G}} = (\mathcal{V}, \mathcal{E}, \widetilde{\mathcal{W}})$ based on the actual status of visited road segments. These real-life updates shared by MDRU will enable other MDRUs to avoid including closed road segments in the developed probabilistic approach when they need to rerun SPA following a dead end.

The process flow for the proposed network model of the post-earthquake scenario and MDRUs routing algorithm for accessing the reachable closest location of the collapsed BSs is summarized in Algorithm 1, wherein lines 1-3 define the scenario of Manhattan environment, network facilities, and earthquake parameters. The post-earthquake modeling starts with running the CY14 earthquake model in line 4. After computing the parameters (μ and β) of the PGA distribution in line 5, the fragility function ($F_R(PGA)$) is calculated in line 6. Thereafter, the set of collapsed buildings and accordingly set of destroyed BSs, $\mathcal{N}$, are identified in line 7. The PDF of debris width, $f_\Omega(\omega)$, and the road closure probabilities, $\mathcal{P}(s^m_{\upsilon,\nu} = 0)$, are computed in lines 8 and 9, respectively.

Following the post-earthquake modeling, the probabilistic graph model with logarithmic weights, $\widetilde{\mathcal{G}}$, is generated in line 10. The MDRUs routing algorithm runs in parallel for every MDRU$_n$ with initialization of source node, s_n, and destination nodes, $\mathcal{T}_n$. Nodes v_k and d^t_n are set as the initial source and destination node in lines 13 and 14, respectively. A while loop between lines 15 and 28 runs until observing that there is no path to reach the destination, which is represented as $v_k \rightsquigarrow d^t_n \neq \infty$, or reaching one of the desired locations, i.e., $v_k \notin \mathcal{T}_n$. DIJKSTRA$(v_k, d^t_n, \widetilde{\mathcal{G}}(\mathcal{V}, \mathcal{E}, \widetilde{\mathcal{W}}))$ runs as an SPA to solve the problem in (24) for finding optimal path, $v_k \rightarrowtail d^t_n$, in line 16. Then, $\mathcal{V}^\star = \{v^\star \in v_k \rightarrowtail d^t_n\}$ is defined as the set of $V^\star$ vertices to be visited from $v_k \rightarrowtail d^t_n$ in line 17.

MDRU$_n$ starts its journey between lines 18 and 27, wherein if the road segment is open in reality, i.e., $\epsilon_{\mathcal{V}^\star\{i\},\mathcal{V}^\star\{i+1\}} == 0$, MDRU$_n$ moves to the next vertex $\mathcal{V}^\star\{i+1\}$ in line 21. Otherwise, the last visited vertex, $\mathcal{V}^\star\{i\}$, is defined as a new source node to be used for one more DIJKSTRA$(v_k, d^t_n, \widetilde{\mathcal{G}}(\mathcal{V}, \mathcal{E}, \widetilde{\mathcal{W}}))$ in a new iteration of the while loop. In both cases, the weight of the considered road segment is updated to the actual weight ($\tilde{\omega}^{\mathcal{V}^\star\{i+1\}}_{\mathcal{V}^\star\{i\}} \leftarrow 0$ or ∞) in line 20 and 23, respectively. Thanks to these updated weights, other MDRUs will be able to calculate more accurate routes with real-life deterministic weights.

Following the termination of the while loop, the algorithm deploys MDRU$_n$ at d^t_n if they reach the desired location in the neighborhood of the collapse BSs in line 30. On the other hand, line 31 refers to the possible case where while loop is terminated without reaching vertices neighboring BS$_n$, $v_k \rightarrowtail d^t_n = \infty$. In such a scenario, we consider the sub-optimal MDRU deployment by taking the inter-cell

Algorithm 1 The Proposed Probabilistic MDRUs Routing

Initialization
1: Define Manhattan environment: R, R_{B}, R_{R},R_{S},R_{Q} and Q, γ
2: Define network facilities: R_{M}, V_{d}, V_{h}, P_{V}, P_{T}, BW, σ_{s}, η
3: Define earthquake parameters: χ, M_q, R_{ss}, V_{s30}, Z_{10}, δ, $\vec{\theta}$, T
Post – Earthquake Modeling
4: Run the CY14 model with NGA-West2 dataset as per (5)
5: $\mu \leftarrow$ (6), $\beta \leftarrow$ (7) *// compute PGA distribution parameters*
6: $F_R(PGA) \leftarrow$ (8) *// compute fragility function*
7: $\mathcal{N} \leftarrow$ as per $\mathcal{P}_C$ in (11) *// identify set of collapsed buildings and BSs*
8: $f_\Omega(\omega) \leftarrow$ as per (13) *// obtain PDF of debris width*
9: $\mathcal{P}(s^m_{\upsilon,\nu} = 0) \leftarrow$ as per (19)-(20) *// compute road closure probabilities*
Routing MDRUs
10: $\widetilde{\mathcal{G}} \leftarrow (\mathcal{V}, \mathcal{E}, \widetilde{\mathcal{W}})$ *// generate probabilistic road graph*
11: **parfor** n = 1 : N **do** *// MDRUs start routing in parallel*
12: Define initial source node s_n and destination nodes $\mathcal{T}_n$
13: $v_k \leftarrow s_n$ *// set initial source node*
14: $d^t_n \leftarrow \mathcal{T}_n\{1\}$ *// set the destination node*
15: **while** $v_k \rightsquigarrow d^t_n \neq \infty \vee v_k \notin \mathcal{T}_n$ **do**
16: $v_k \rightarrowtail d^t_n \leftarrow$ DIJKSTRA$\big(v_k, d^t_n, \widetilde{\mathcal{G}}(\mathcal{V}, \mathcal{E}, \widetilde{\mathcal{W}})\big)$ *// solve (24)*
17: $\mathcal{V}^\star \leftarrow v_k \rightarrowtail d^t_n$ *// set of $V^\star$ vertices to be visited*
18: **for** $i = 1 : V^\star - 1$ **do** *// MDRU$_n$ starts its journey*
19: **if** $\epsilon_{\mathcal{V}^\star\{i\},\mathcal{V}^\star\{i+1\}} == 0$ **then** *// road segment is open in reality*
20: $\tilde{\omega}^{\mathcal{V}^\star\{i+1\}}_{\mathcal{V}^\star\{i\}} \leftarrow 0$ *// update prob. weight with actual weight*
21: $v_k \leftarrow \mathcal{V}^\star\{i+1\}$ *// update latest position of MDRU$_n$*
22: **else** *// road segment is blocked in reality*
23: $\tilde{\omega}^{\mathcal{V}^\star\{i+1\}}_{\mathcal{V}^\star\{i\}} \leftarrow \infty$ *// update prob. weight with actual weight*
24: $v_k \leftarrow \mathcal{V}^\star\{i\}$ *// define new source node to last visited vertex*
25: **break**
26: **end if**
27: **end for**
28: **end while**
29: **if** $v_k \in \mathcal{T}_n$ **then** *// MDRU$_n$ reached to target BS$_n$*
30: Deploy MDRU$_n$ at v_k
31: **else** *// decide on sub-optimal deployment*
32: Find $v_{\min}$ *// vertex with the min. Euclidean distance to d^t_n*
33: **if** $\Delta < \Gamma$ **then** *// tolerable inter-cell interference*
34: Deploy MDRU$_n$ at $v_{\min}$
35: **else** *// extreme inter-cell interference*
36: Omit MDRU$_n$ from network
37: **end if**
38: **end if**
39: **end parfor**

interference tolerance distance, Γ, into account. To this aim, MDRU$_n$ first identifies all visited vertices throughout the journey and determines the vertex with the shortest Euclidean distance, Δ, to the BS$_n$, $v_{\min}$. If the inter-cell interference is tolerable, i.e., $\Delta < \Gamma$,[2] MDRU$_n$ is deployed at $v_{\min}$ in line 34, otherwise omitted from network in line 36. Noting that initialization and post-earthquake modeling can be executed offline, the routing complexity for MDRU is governed by the times DIJKSTRA executed. Accordingly, the overall time complexity is given by $\mathcal{O}(K(V+E)\ \log V)$, where K is the total number of iterations of the while loop.[3] The original problem, involving service recovery with unknown road blockages, is non-convex and lacks a polynomial-time optimal solution. Our heuristic method reduces complexity by focusing on feasible, rather than fully optimal, path solutions.

In conclusion, inspired by the statistical insights gleaned from our developed model on the stochastic city model after the earthquake (as outlined in Section III), Dijkstra's approach prioritizes both shortest path and time. Unlike traditional uniform weight distance-based algorithms, it takes into account the probability of road closure along the route and its contributing factors, including building heights, road width, probability of building collapse, and probability of segment closure. Exploiting the earthquake city model helps to reduce the time needed to restore the network functionality by effectively avoiding statistically predictable blocked roads and backtracks.

V. NUMERICAL RESULTS

In this section, we present an extensive set of simulations to validate the derived statistical model for the city and network operation after the earthquake hits and evaluate the performance gains achieved by adopting the proposed MDRUs routing solution. In the considered simulation setup, the default model parameters' values for the Manhattan city and network deployment are selected to match their counterparts in [34], [40]. Specifically, we set the block size and road width to $R_{\mathrm{B}} = 75$ m and $R_{\mathrm{R}} = 15$ m [34], respectively, where, each road accommodates $R_{\mathrm{S}} = 4$ buildings, and avenues are regularly placed with $Q = 1.25$ and $R_{\mathrm{Q}} = 8$ roads- separation intervals along both the X and Y axes. Moreover, building heights are generated using $\gamma = 11.5$, while the distance between BSs is set at 1000 m ($R_{\mathrm{M}} = 577$ m) [34]. The number of destination points, which are the nearest vertices to collapsed BSs for each MDRU, is defined as $|\mathcal{T}_n| = 4$. The threshold distance for sub-optimal MDRU deployment is defined as $\Gamma = R_{\mathrm{M}}\sqrt{3}/2$. Furthermore, the antenna height of the MDRUs and the vehicle width are set as $V_{\mathrm{h}} = 9$ m and $V_{\mathrm{d}} = 3.5$ m, respectively [23]. All radio units operate with a transmit power of 40 dBm and a bandwidth of 20 MHz [40]. As for the wireless communication environment, we have $\eta = 4$ representing the path loss exponent, and $\sigma_{\mathrm{s}} = 3$ indicating the shadowing fading standard deviation [40].

For the earthquake model parameters, we utilize the CY14 earthquake model based on the NGA-West2 dataset [36]. Key parameters include $M_{\underrightarrow{q}} = 6.5$, $R_{ss} = 10$ km, $V_{s30} = 500$, $Z_{10} = 999$, $\delta = 90$, $\vec{\theta} = 0$, and $T = 0$. The study covers an extensive area of 200 km^2 ($R = 14140$ m), with the earthquake epicenter located at the top right corner at coordinates $\chi = (7.5$ km, 7.5 km$)$. To ensure high spatial resolution, the heat maps are generated using 40,000 uniformly distributed sample points. These measurement points were not representative of UEs deployment but were strategically placed to evaluate network performance, including SINR distribution and service availability, across the spatial domain. For robust statistical analysis, 10^5 earthquake realizations are simulated, incorporating the derived statistical models to assess the associated damage to network infrastructure and road blockages.

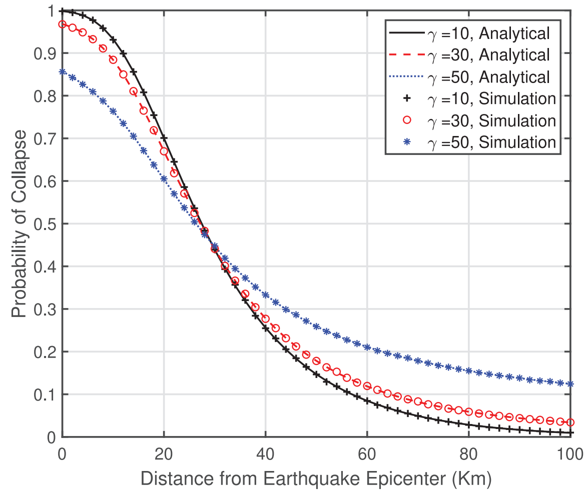

FIGURE 6. **Building collapse probability analytical vs Monte Carlo simulation for different γ values.**

A. POST-EARTHQUAKE DAMAGE MODEL VERIFICATION

Figure 6 illustrates the probability of building collapse as a function of the distance from the earthquake epicenter for various γ values. The close alignment between the analytical curves derived from (11) and the Monte Carlo simulation results validates the accuracy of (11). As expected, the probability of building collapse decreases with increasing distance from the epicenter, corresponding to a greater source-to-site distance. This trend is attributed to the lower likelihood of encountering higher PGA values as the measurement site moves further from the earthquake epicenter.

In Fig. 7, we compare the empirical PDF of debris width with the closed-form expression given in Lemma 1 for various building heights. During the Monte Carlo validation process, random building heights were generated using a Rayleigh distribution to represent the variability in building sizes within the affected area. Additionally, debris width

[2] Γ should be less than the cell radius of BSs so that MDRU$_n$ is not deployed within the cell-coverage of other BSs.

[3] It is worth noting that determining K is non-trivial. In order to guarantee a certain complexity, one can predetermine K as the maximum iteration number to use as an additional termination condition.

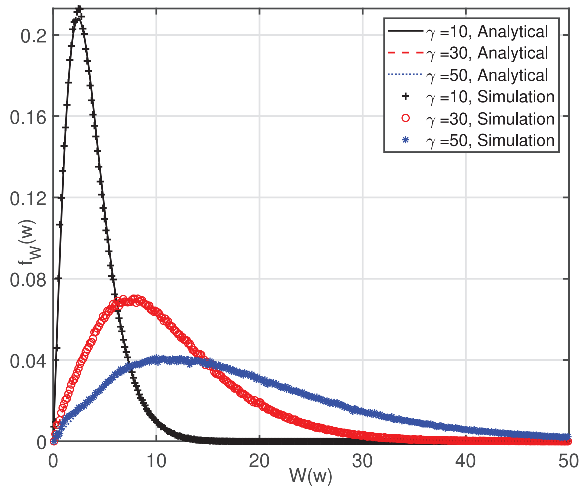

FIGURE 7. Debris width PDF analytical vs Monte Carlo simulation.

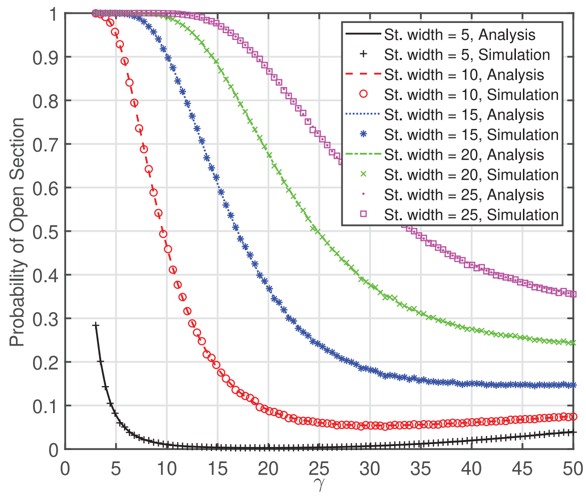

FIGURE 8. Open section probability analytical vs Monte Carlo simulation for various γ values.

values were generated following a triangular distribution, as described in (12), to model the range of debris extension resulting from building collapse. The close match between the empirical and analytical results across all building heights verifies the accuracy of the mathematical analysis and the formula in (13).

Figure 8 presents the probability of an open road section as a function of γ for different street widths. The plot demonstrates that the analytical formulas in (19) and (20) are in exact agreement with the results obtained through Monte Carlo simulations. It is evident from Fig. 8 that as building heights increase, the probability of road section blockage–and consequently, the blockage of the entire road segment–also increases. Furthermore, wider road sections are shown to be less prone to blockage than narrower sections, as depicted in Fig. 8, due to the larger passage distance available for emergency vehicles. Finally, in Fig. 9, the spatial distribution of the probability of building collapse is depicted for an earthquake with a magnitude of $M_q = 6.5$.

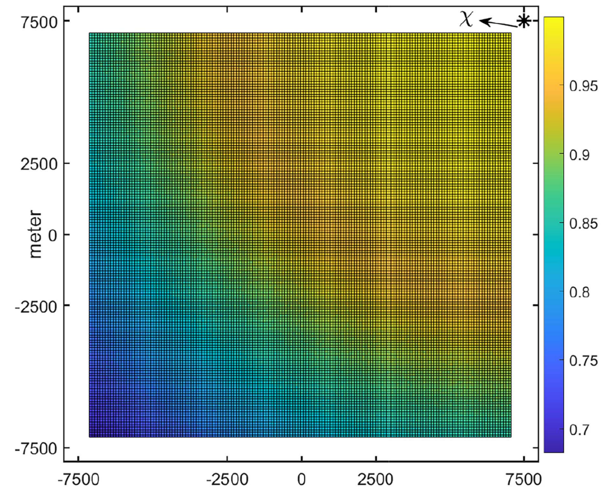

FIGURE 9. The probability of building collapse with our adopted PGA value and fragility stochastic model.

B. NETWORK RESTORATION PERFORMANCE

In this subsection, we elaborate on the numerical results for network recovery, focusing on the SINR across various metrics: mean and quantile values, the probability of network service availability at different SINR thresholds, and capacity comparisons between the before earthquake (BEQ), after earthquake (AEQ), and response earthquake (REQ) scenarios.

Figure 10 presents the SINR heat map for a single realization across different scenarios. The BEQ scenario shows uniform SINR performance throughout the area, in contrast to the AEQ and REQ scenarios. In the AEQ scenario, despite generally poor SINR performance, a notable increase is observed in certain areas where surviving BSs lose their neighboring BSs. This improvement is primarily due to the reduction in interference signals from adjacent base stations. However, as illustrated in Fig. 10 (c), road blockages can restrict the coverage of MDRUs, potentially resulting in coverage gaps, particularly near χ, as seen in this single realization for the REQ scenario.

The SINR performance (in dB) for the BEQ, AEQ, and REQ scenarios is further analyzed at different quantile levels in Fig. 11 (a)-(b)-(c), (d)-(e)-(f), and (g)-(h)-(i), respectively, following the order: 5%, 50%, and 95%. The BEQ scenarios consistently exhibit uniform SINR, with variations arising primarily from communication channels and building heights, leading to minimal impact across different quantile values. In contrast, the AEQ scenario shows significant fluctuations in SINR performance. The 5% and 50% quantiles yield the poorest SINR outcomes compared to the other scenarios, while the 95% quantile in the AEQ scenario demonstrates the best SINR performance, except near the earthquake epicenter. The exceptionally high SINR value at the 95% quantile in the AEQ scenario can be better understood by examining a single realization, as shown in Fig. 10 (b).

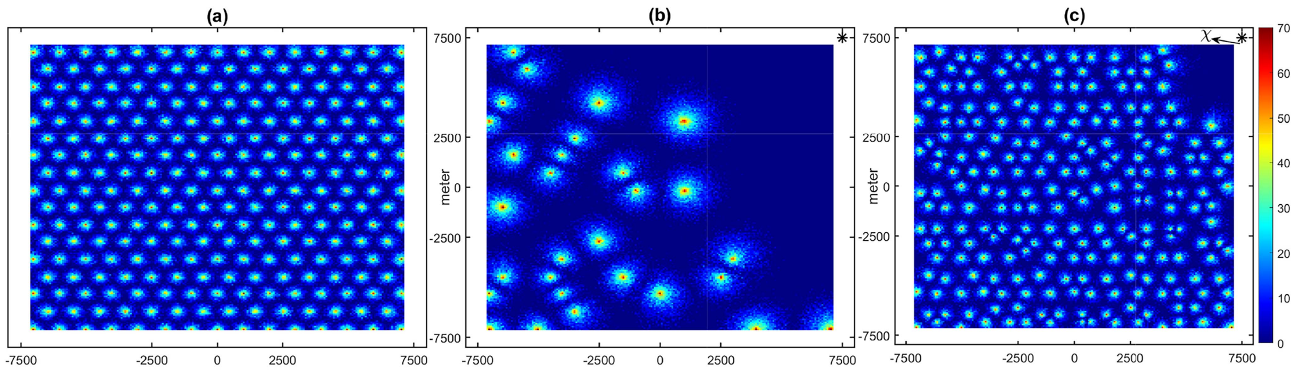

FIGURE 10. SINR performances (dB) with single realization in 200 km^2 area where the earthquake epicenter at (7.5 km,7.5 km) for (a) BEQ, (b) AEQ, and (c) REQ scenarios.

The REQ scenario, however, does not consistently perform well, as indicated by the 5% quantile in Fig. 11 (g). This inconsistency is due to the MDRUs being unable to reach optimal locations because of road blockages. Similarly, a degradation in SINR performance is observed across all REQ scenarios at different quantile values, particularly from the farthest area of the earthquake epicenter to χ since MDRUs encounter higher road blockage probabilities closer to the χ. Additionally, the SINR performance in the REQ scenario improves with higher quantile values. The SINR pattern in REQ scenarios also differs from those in BEQ and AEQ scenarios due to the deployment of MDRUs.

The average SINR (dB) comparisons are presented in Fig. 12. The spatial distribution of the earthquake's impact on SINR performance is evident when comparing the BEQ and AEQ scenarios. The presence of BS cell edges in the hexagonal uniform deployment becomes apparent through the SINR improvement at these edges in the AEQ scenario, which results from reduced inter-cell interference (ICI). The SINR improvement in the REQ scenario compared to AEQ is highlighted in Fig. 12 (b), where the deployment of MDRUs contributes to enhanced SINR performance. The comparison between BEQ and REQ, as shown in Fig. 12 (c), demonstrates that the REQ scenario with MDRUs compensates for earthquake damage, resulting in an average SINR performance of approximately 0 dB across the considered area.

Figure 13 illustrates the probability of network service availability for SINR thresholds of −4 dB, 0 dB, and 4 dB, organized as (a)-(b)-(c) for BEQ, (d)-(e)-(f) for AEQ, and (g)-(h)-(i) for REQ scenarios. The Fig. 13 (d)-(e)-(f) clearly reflect the impact of the earthquake on the communication system. In AEQ scenarios, network service availability drops by approximately 35%, 25%, and 15% on average for the half of the area closest to χ, corresponding to SINR thresholds of −4 dB, 0 dB, and 4 dB, respectively. The efficacy of the proposed approach in restoring network performance in the REQ scenario is demonstrated in Fig. 13 (g)-(h)-(i). Compared to the BEQ scenario shown in Fig. 13 (a)-(b)-(c), the REQ scenario shows significant recovery in network service availability across all threshold levels. However, the probabilities differ from the BEQ scenario due to the absence of a pure uniform deployment of MDRUs. Additionally, network service availability near the χ location exhibits slightly lower performance compared to areas farther from the epicenter, due to higher road blockages. For example, in the scenario with a −4 dB threshold shown in Fig. 13 (g), the area farthest from the earthquake epicenter nearly maintains full network service, similar to the BEQ scenario in Fig. 13 (a). However, this consistency is not observed in the area closer to the earthquake epicenter.

The simulation results for the average capacity performance across the three scenarios are presented in Fig. 14. The evaluation, based on CDF curves, shows that the REQ scenario performs similarly to the BEQ scenario for capacities between 0.3 and 0.8 Mbps. However, for the remaining capacity values, BEQ slightly outperforms REQ. This difference in performance is mainly due to the imperfect uniform deployment of MDRUs and the absence of MDRU deployments in unreachable locations, particularly those closest to the earthquake epicenter. The AEQ scenario exhibits the poorest capacity performance, which is attributed to the collapse of BSs and the subsequent loss of radio resources, resulting in limited resource sharing. Although AEQ can produce very high SINR values, as seen in Fig. 11 (f) with the 95% quantile, the actual capacity performance is compromised due to the limited availability of resources.

Lastly, the performance of the proposed routing algorithm across different earthquake magnitudes is evaluated. As a benchmark for the routing method, the traditional Dijkstra with uniform weight distance-based algorithm is considered. The travel time results from both approaches are calculated and compared in Fig. 15. In every scenario, the proposed routing algorithm demonstrates superior performance by statistically predicting blocked roads and minimizing backtracking. For minor earthquakes, where road blockages are minimal, the earthquake city model is not fully exploited. However, notable improvements are observed after magnitude 5, with performance enhancements reaching approximately %31 compared to the distance-based approach. Moreover, it's important to note that the proposed algorithm's performance improvement does not always increase with higher magnitudes due to the dense road blockages within the city. Nevertheless, the proposed

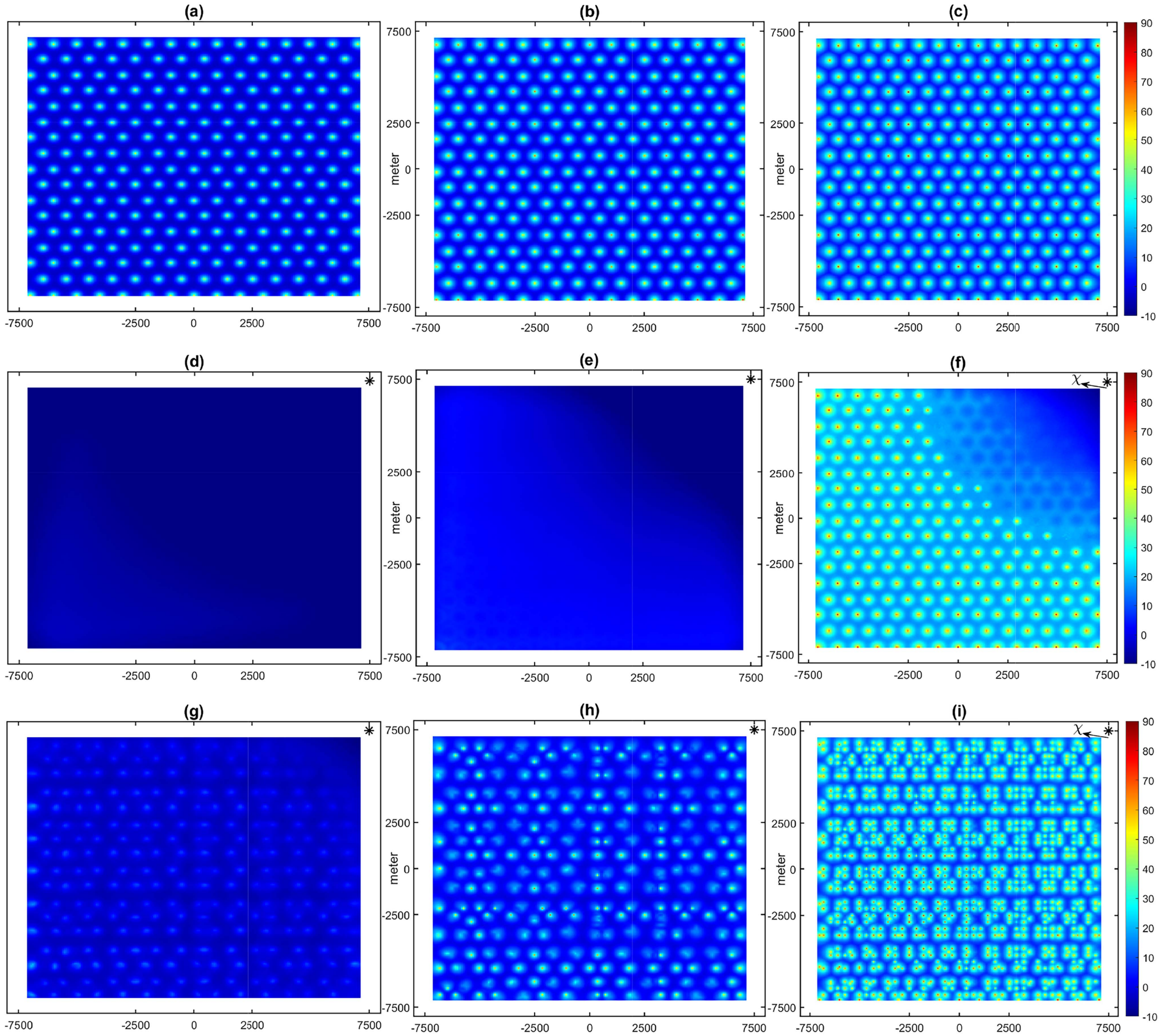

FIGURE 11. SINR performances (dB) for BEQ (a)-(b)-(c), AEQ (d)-(e)-(f), and REQ (g)-(h)-(i) scenarios at different quantile values with the same order: %5, %50, and %95.

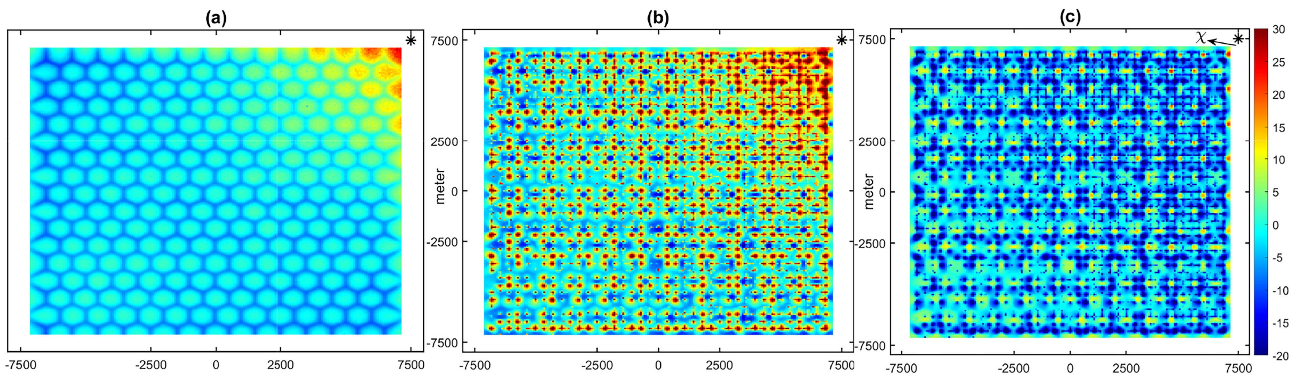

FIGURE 12. Mean SINR (dB) differences for (a) BEQ-AEQ, (b) REQ-AEQ, and (c) BEQ-REQ.

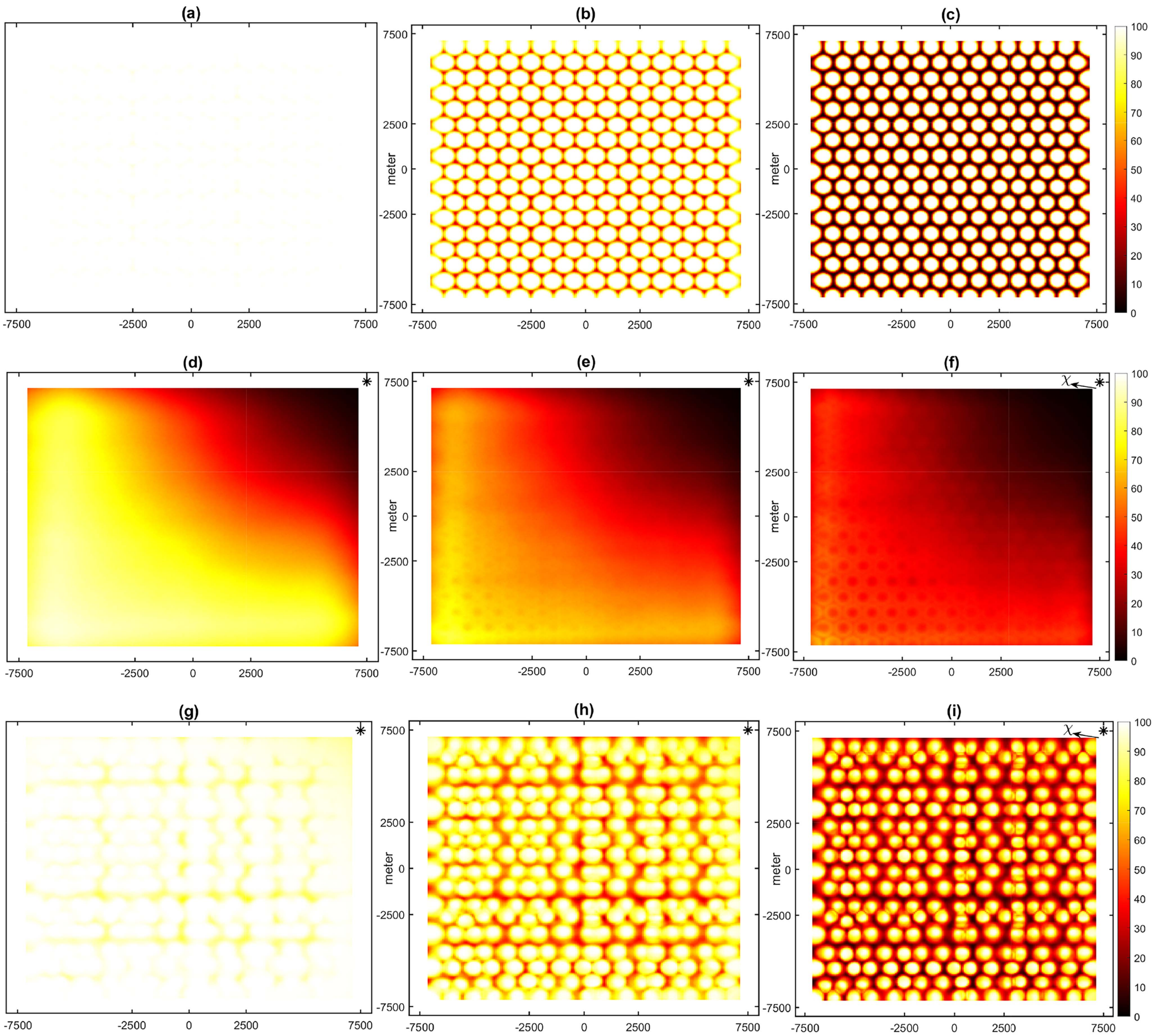

FIGURE 13. The availability percentage of network service for BEQ (a)-(b)-(c), AEQ (d)-(e)-(f), and REQ (g)-(h)-(i) scenarios with the same order of thresholds −4 dB, 0 dB, and 4 dB.

method effectively routes the MDRUs to facilitate network restoration by reducing travel distance and subsequently reducing overall travel time.

VI. CONCLUSION

In this paper, we proposed a realistic post-earthquake network model that serves as a foundational framework for future research on post-earthquake wireless communication network planning and optimization. Notably, this work is the first to jointly present a seismic-based city and network destruction model, which is then utilized for the routing and deployment of MDRUs to restore network coverage. Through extensive simulations, we validated the accuracy of the derived city and network destruction models. Furthermore, we demonstrated the effectiveness of the proposed MDRUs routing approach in restoring network coverage to pre-earthquake levels in most regions, while significantly reducing network restoration time compared to road blockage-agnostic shortest-path routing method. Looking ahead, we suggest that future research should consider the effects of cascaded power outages and backhaul infrastructure damage. Additionally, by leveraging earthquake spatial distribution data, ABSs could be explored for deployment in areas where MDRUs have low accessibility. AI techniques could also be explored to model network collapse and optimize routing algorithms in post-disaster environments. Moreover, the development of new channel models based on debris characteristics and the altered city landscape post-destruction could further enhance the realism and applicability of post-earthquake communication network models. Lastly, by collaborating with relevant stakeholders or utilizing field test data, further validation of the proposed models can be provided.

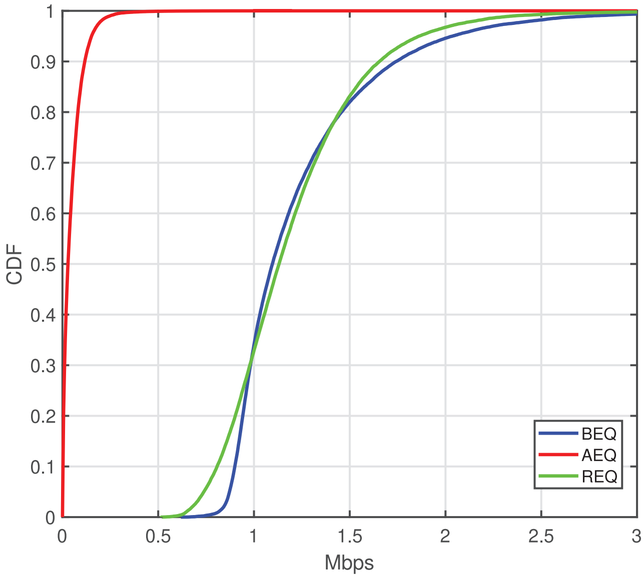

FIGURE 14. Capacity comparison for different scenarios.

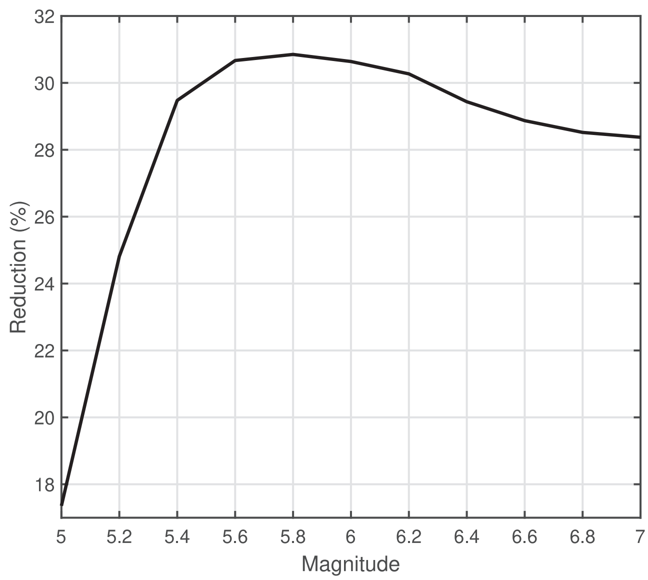

FIGURE 15. Travelling time performance of the proposed routing algorithm against the traditional distance-based approach for different earthquake magnitudes.

APPENDIX A
PROOF OF LEMMA 1

To derive the distribution function of debris width stated in (13), we start with the conditional probability of debris width given in (12). Since in this study random building heights are assumed, we integrate with respect to h, to obtain the PDF of debris width $f_\Omega(\omega)$ as below:

$$
\begin{aligned}
f_\Omega(\omega) &= \int_0^\infty f(\omega,h) f_H(h)dh \\
&\overset{(a)}{=} \int_{4\omega}^{8\omega} f_1(\omega,h)f_H(h)dh + \int_{2\omega}^{4\omega} f_2(\omega,h)f_H(h)dh \\
&\overset{(b)}{=} \int_{4\omega}^{8\omega} \frac{2\left(\omega-\frac{h}{8}\right)}{\left(\frac{h}{2}-\frac{h}{8}\right)\left(\frac{h}{4}-\frac{h}{8}\right)} \frac{h}{\gamma^2} \exp\left(-\frac{h^2}{2\gamma^2}\right)dh \\
&\quad + \int_{2\omega}^{4\omega} \frac{2\left(\frac{h}{2}-\omega\right)}{\left(\frac{h}{2}-\frac{h}{8}\right)\left(\frac{h}{2}-\frac{h}{8}\right)} \frac{h}{\gamma^2} \exp\left(-\frac{h^2}{2\gamma^2}\right)dh \\
&\overset{(c)}{=} \frac{8}{3\gamma^2}\left(8\omega \mathrm{ei}\left(\frac{-32\omega^2}{\gamma^2}\right) - 12\omega \mathrm{ei}\left(\frac{-8\omega^2}{\gamma^2}\right)\right. \\
&\quad + 4\omega \mathrm{ei}\left(\frac{-2\omega^2}{\gamma^2}\right) - \sqrt{2\pi}\gamma \mathrm{erf}\left(\frac{4\sqrt{2}\omega}{\gamma^2}\right) \\
&\quad \left. +3\sqrt{2\pi}\gamma \mathrm{erf}\left(\frac{2\sqrt{2}\omega}{\gamma^2}\right) + 2\sqrt{2\pi}\gamma \mathrm{erf}\left(\frac{\sqrt{2}\omega}{\gamma^2}\right)\right) \\
&\overset{(d)}{=} \frac{8}{3\gamma^2}\omega \sum_{p=0}^{2} a_p \mathrm{ei}\left(\frac{(-2)^{2p+1}}{\gamma^2}\omega^2\right) \\
&\quad + \frac{8\sqrt{2\pi}}{3\gamma} \sum_{q=0}^{2} b_q \mathrm{erf}\left(\frac{2^q\sqrt{2}}{\gamma^2}\omega\right),
\end{aligned}
\tag{25}
$$

where (a) follows from the conditional distribution function of debris width given a building height defined for different intervals as in (12), (b) follows from explicitly substituting the conditional probability of the debris width described by the triangular distribution function and probability of the building height defined by a Rayleigh distribution, (c) follows the integral solution by using the substitution method as explained in ([41], chap. 5) and after that solving the non-elementary integrals [42], and (d) transition represents the general result as stated in (13). Here, a_p and b_q, are the corresponding coefficients following from (c) transition.

APPENDIX B
PROOF OF LEMMA 2

Let d_{th} be the threshold distance for the road section to be open expressed as the difference between the road width R_R and emergency vehicle width V_d. For a Manhattan-grid city model with Rayleigh-distributed building heights parameter γ the probability that a $s^m_{\upsilon,\nu}$ of the road segment $\epsilon_{\upsilon,\nu}$ remains unobstructed given that two buildings on opposite sides collapsed can be expressed as

$$
\begin{aligned}
&\mathcal{P}\left(s^m_{\upsilon,\nu}=0|B_\mathrm{C},B'_\mathrm{C}\right) = \int_0^{d_\text{th}}\int_0^{d'_\text{th}} f_\Omega(\omega)f_\Omega(\omega')d\omega d\omega' \\
&\overset{(a)}{=} \int_0^{d_\text{th}} f_\Omega(\omega')\frac{1}{3\gamma^2}\left(\left(-3\gamma^2+\exp\left(-\frac{32d'^2_\text{th}}{\gamma^2}\right)\gamma^2\right.\right. \\
&\quad - 6\exp\left(-\frac{8d'^2_\text{th}}{\gamma^2}\right)\gamma^2 + 8\exp\left(-\frac{2d'^2_\text{th}}{\gamma^2}\right)\gamma^2 \\
&\quad + 16d_\text{th}\sqrt{2\pi}\gamma\mathrm{erf}\left(\frac{\sqrt{2}d'_\text{th}}{\gamma}\right) - 24d_\text{th}\sqrt{2\pi}\gamma\mathrm{erf}\left(\frac{2\sqrt{2}d'_\text{th}}{\gamma}\right) \\
&\quad + 8d_\text{th}\sqrt{2\pi}\gamma\mathrm{erf}\left(\frac{4\sqrt{2}d'_\text{th}}{\gamma}\right) + 16d^2_\text{th}\Gamma\left(0,\frac{2d'^2_\text{th}}{\gamma^2}\right) \\
&\quad \left. - 48d^2_\text{th}\Gamma\left(0,\frac{8d'^2_\text{th}}{\gamma^2}\right) + 32d^2_\text{th}\Gamma\left(0,\frac{32d'^2_\text{th}}{\gamma^2}\right)\right) \\
&\quad - 8\omega'\left(2\sqrt{2}\gamma\mathrm{erf}\left(\frac{\sqrt{2}d'_\text{th}}{\gamma}\right) - 3\sqrt{2\pi}\gamma\mathrm{erf}\left(\frac{2\sqrt{2}d'_\text{th}}{\gamma}\right)\right.
\end{aligned}
$$

$$+\sqrt{2\pi}\gamma\,\mathrm{erf}\left(\frac{4\sqrt{2}d'_{\mathrm{th}}}{\gamma}\right)+4d_{\mathrm{th}}\Gamma\left(0,\frac{2d'^2_{\mathrm{th}}}{\gamma^2}\right)$$
$$-12d_{\mathrm{th}}\Gamma\left(0,\frac{8d'^2_{\mathrm{th}}}{\gamma^2}\right)+8d_{\mathrm{th}}\Gamma\left(0,\frac{32d'^2_{\mathrm{th}}}{\gamma^2}\right)\Bigg)$$
$$+16\omega'^2\left(\Gamma\left(0,\frac{2d'^2_{\mathrm{th}}}{\gamma^2}\right)-3\Gamma\left(0,\frac{8d'^2_{\mathrm{th}}}{\gamma^2}\right)+2\Gamma\left(0,\frac{32d'^2_{\mathrm{th}}}{\gamma^2}\right)\right)\Bigg)\Bigg)$$
$$\overset{(b)}{=}\int_0^{d_{\mathrm{th}}} f_\Omega(\omega')\Bigg(\frac{1}{3}\sum_{i=0}^{2}c_i\exp\left(\frac{(-2)^{2i+1}}{\gamma^2}d'_{\mathrm{th}}\right)$$
$$+\frac{\sqrt{2\pi}}{3\gamma}d_{\mathrm{th}}\sum_{j=0}^{2}c_j\mathrm{erf}\left(\frac{2^j\sqrt{2}}{\gamma}d'_{\mathrm{th}}\right)$$
$$+\frac{1}{3\gamma^2}d^2_{\mathrm{th}}\sum_{k=0}^{2}c_k\Gamma\left(0,\frac{2^{2k+1}}{\gamma^2}d'^2_{\mathrm{th}}\right)$$
$$-\frac{8}{3\gamma^2}\omega'\Bigg(\sqrt{2\pi}\gamma\sum_{l=0}^{2}c_l\mathrm{erf}\left(\frac{2^l\sqrt{2}}{\gamma}d'_{\mathrm{th}}\right)$$
$$+\frac{1}{3\gamma^2}d_{\mathrm{th}}\sum_{m=0}^{2}c_m\Gamma\left(0,\frac{2^{2m+1}}{\gamma^2}d'^2_{\mathrm{th}}\right)\Bigg)$$
$$+\frac{16}{3\gamma^2}\omega'^2\sum_{n=0}^{2}c_n\Gamma\left(0,\frac{2^{2n+1}}{\gamma^2}d'^2_{\mathrm{th}}\right)-1\Bigg)d\omega', \tag{26}$$

where (a) follows the solution of the inner integral by using the substitution technique and computing the non-elementary integrals, and (b) transition represents the final result as stated in (19). For simplicity the notation $d'_{\mathrm{th}}=d_{\mathrm{th}}-\omega'$ is performed where $(')$ refers to the opposite side building and c_i, c_j, c_k, c_l, c_m, c_n are the respective coefficients coming from (a).

On the other hand, the probability that a $s^m_{\upsilon,\nu}$ of the road segment $\epsilon_{\upsilon,\nu}$ remains open given that a single building on only one side of the road segment collapsed is provided by

$$\mathcal{P}\left(s^m_{\upsilon,\nu}=0|B_{\mathrm{C}},B'_{\bar{\mathrm{C}}}\right)=\int_0^{d_{\mathrm{th}}}f_\Omega(\omega)d\omega$$
$$\overset{(a)}{=}\frac{1}{3\gamma^2}\Bigg(\gamma^2\exp\left(\frac{-32d^2_{\mathrm{th}}}{\gamma^2}-1\right)$$
$$-256d^2_{\mathrm{th}}\Gamma\left(0,\frac{32d^2_{\mathrm{th}}}{\gamma^2}\right)-2\Bigg(3\gamma^2\exp\left(\frac{-8d^2_{\mathrm{th}}}{\gamma^2}-1\right)$$
$$-32d^2_{\mathrm{th}}\Gamma\left(0,\frac{8d^2_{\mathrm{th}}}{\gamma^2}\right)\Bigg)+8\Bigg(\gamma^2\exp\left(\frac{-2d^2_{\mathrm{th}}}{\gamma^2}-1\right)$$
$$-2d^2_{\mathrm{th}}\Gamma\left(0,\frac{d^2_{\mathrm{th}}}{\gamma^2}\right)\Bigg)-2\Bigg(\gamma^3\exp\left(\frac{-32d^2_{\mathrm{th}}}{\gamma^4}-1\right)$$
$$+4d_{\mathrm{th}}\sqrt{2\pi}\gamma\,\mathrm{erf}\left(\frac{4\sqrt{2}d_{\mathrm{th}}}{\gamma^2}\right)\Bigg)+12\Bigg(\gamma^3\exp\left(\frac{-8d^2_{\mathrm{th}}}{\gamma^4}-1\right)$$
$$+2d_{\mathrm{th}}\sqrt{2\pi}\gamma\,\mathrm{erf}\left(\frac{2\sqrt{2}d_{\mathrm{th}}}{\gamma^2}\right)\Bigg)+16\Bigg(\gamma^3\exp\left(\frac{-2d^2_{\mathrm{th}}}{\gamma^4}-1\right)$$
$$+d_{\mathrm{th}}\sqrt{2}\gamma\,\mathrm{erf}\left(\frac{\sqrt{2}d_{\mathrm{th}}}{\gamma^2}\right)\Bigg)\Bigg)$$
$$\overset{(b)}{=}\frac{1}{3}\sum_{u=0}^{2}c_u\exp\left(\frac{(-2)^{2u+1}}{\gamma^2}d^2_{\mathrm{th}}-1\right)$$
$$+\frac{1}{3}\gamma\sum_{v=0}^{2}c_v\exp\left(\frac{(-2)^{2v+1}}{\gamma^4}d^2_{\mathrm{th}}-1\right)$$
$$+\frac{\sqrt{2\pi}}{3\gamma}d_{\mathrm{th}}\sum_{y=0}^{2}c_y\mathrm{erf}\left(\frac{2^y\sqrt{2}}{\gamma^2}d_{\mathrm{th}}\right)$$
$$+\frac{2}{3\gamma^2}d^2_{\mathrm{th}}\sum_{z=0}^{2}c_z\Gamma\left(0,\frac{2^{2z+1}}{\gamma^2}\right), \tag{27}$$

where (a) transition follows from integrating the debris width PDF found as in (13) by using the integral substitution method and evaluating the non-elementary integrals, (b) represents the general expression stated in (20), and the terms c_u, c_v, c_y, c_z are the corresponding coefficients coming from (a) transition.

ACKNOWLEDGMENT

The authors would like to thank D. Merve for her valuable assistance in creating Fig. 1 and Fig. 2.

REFERENCES

[1] M. Matracia, M. A. Kishk, and M.-S. Alouini, "On the topological aspects of UAV-assisted post-disaster wireless communication networks," *IEEE Commun. Mag.*, vol. 59, no. 11, pp. 59–64, Nov. 2021.

[2] M. M. Hasan et al., "Search and rescue operation in flooded areas: A survey on emerging sensor networking-enabled IoT-oriented technologies and applications," *Cogn. Syst. Res.*, vol. 67, pp. 104–123, Jun. 2021.

[3] M. B. Janjua, A. E. Duranay, and H. Arslan, "Role of wireless communication in healthcare system to cater disaster situations under 6G vision," *Front. Commun. Netw.*, vol. 1, Dec. 2020, Art. no. 12054.

[4] H.-C. Jang, Y.-N. Lien, and T.-C. Tsai, "Rescue information system for earthquake disasters based on MANET emergency communication platform," in *Proc. Int. Conf. Wireless Commun. Mobile Comput. Connect. World Wirelessly*, 2009, pp. 623–627.

[5] G. C. Deepak, A. Ladas, Y. A. Sambo, H. Pervaiz, C. Politis, and M. A. Imran, "An overview of post-disaster emergency communication systems in the future networks," *IEEE Wireless Commun.*, vol. 26, no. 6, pp. 132–139, Dec. 2019.

[6] K. Miranda, A. Molinaro, and T. Razafindralambo, "A survey on rapidly deployable solutions for post-disaster networks," *IEEE Commun. Mag.*, vol. 54, no. 4, pp. 117–123, Apr. 2016.

[7] M. Ş. Balaban et al., "Emergency response, and community impact after February 6, 2023 Kahramanmaraş Pazarcık and Elbistan earthquakes: Reconnaissance findings and observations on affected region in Türkiye," *Bull. Earthq. Eng.*, vol. 2024, pp. 1–30, Feb. 2024.

[8] "Kahramanmaraş and Hatay earthquakes report: Presidency of strategy budget," Presidency of Türkiye, 2023. [Online]. Available: chrome-extension://efaidnbmnnnibpcajpcglclefindmkaj/https://www.sbb.gov.tr/wp-content/uploads/2023/03/2023-Kahramanmaras-and-Hatay-Earthquakes-Report.pdf

[9] "February 6 earthquakes 8th month evaluation report: Union of Chambers of Turkish engineers architects," TMMOB, 2023 [Turkish]. [Online]. Available: https://www.tmmob.org.tr/icerik/tmmob-6-subat-depremleri-8-ay-degerlendirmeraporu-yayimlandi

[10] T. Sakano et al., "Bringing movable and deployable networks to disaster areas: Development and field test of MDRU," *IEEE Netw.*, vol. 30, no. 1, pp. 86–91, Jan./Feb. 2016.

[11] T. Gomes et al., "A survey of strategies for communication networks to protect against large-scale natural disasters," in *Proc. 8th Int. Workshop Resilient Netw. Design Model. (RNDM)*, 2016, pp. 11–22.

[12] T. Sakano et al., "Disaster-resilient networking: A new vision based on movable and deployable resource units," *IEEE Netw.*, vol. 27, no. 4, pp. 40–46, Jul./Aug. 2013.

[13] J. Wang, S. Guo, Z. Cheng, P. Li, and J. Wu, "Optimization of deployable base stations with guaranteed QoE in disaster scenarios," *IEEE Trans. Veh. Technol.*, vol. 66, no. 7, pp. 6536–6552, Jul. 2017.

[14] T. Ngo, H. Nishiyama, N. Kato, T. Sakano, and A. Takahara, "A spectrum- and energy-efficient scheme for improving the Utilization of MDRU-based disaster resilient networks," *IEEE Trans. Veh. Technol.*, vol. 63, no. 5, pp. 2027–2037, Jun. 2014.

[15] T. Do-Duy, L. D. Nguyen, T. Q. Duong, S. R. Khosravirad, and H. Claussen, "Joint optimization of real-time deployment and resource allocation for UAV-aided disaster emergency communications," *IEEE J. Sel. Areas Commun.*, vol. 39, no. 11, pp. 3411–3424, Nov. 2021.

[16] M. Matracia, M. A. Kishk, and M.-S. Alouini, "UAV-aided post-disaster cellular networks: A novel stochastic geometry approach," *IEEE Trans. Veh. Technol.*, vol. 72, no. 7, pp. 9406–9418, Jul. 2023.

[17] M. Matracia, M. A. Kishk, and M.-S. Alouini, "Comparing aerial-RIS- and aerial-base-station-aided post-disaster cellular networks," *IEEE Open J. Veh. Technol.*, vol. 4, pp. 782–795, 2023.

[18] S. Zhang and J. Liu, "Analysis and optimization of multiple unmanned aerial vehicle-assisted communications in post-disaster areas," *IEEE Trans. Veh. Technol.*, vol. 67, no. 12, pp. 12049–12060, Dec. 2018.

[19] S. A. R. Naqvi, S. A. Hassan, H. Pervaiz, and Q. Ni, "Drone-aided communication as a key enabler for 5G and resilient public safety networks," *IEEE Commun. Mag.*, vol. 56, no. 1, pp. 36–42, Jan. 2018.

[20] Z. Yao, W. Cheng, W. Zhang, and H. Zhang, "Resource allocation for 5G-UAV-based emergency wireless communications," *IEEE J. Sel. Areas Commun.*, vol. 39, no. 11, pp. 3395–3410, Nov. 2021.

[21] M. Matracia, N. Saeed, M. A. Kishk, and M.-S. Alouini, "Post-disaster communications: Enabling technologies, architectures, and open challenges," *IEEE Open J. Commun. Soc.*, vol. 3, pp. 1177–1205, 2022.

[22] N. Hirokawa and T. Osaragi, "Earthquake disaster simulation system: Integration of models for building collapse, road blockage, and fire spread," *J. of Disaster Res.*, vol. 11, no. 2, pp. 175–187, 2016.

[23] S. Argyroudis, J. Selva, P. Gehl, and K. Pitilakis, "Systemic seismic risk assessment of road networks considering interactions with the built environment," *Comput.-Aided Civil Infrastruct. Eng.*, vol. 30, no. 7, pp. 524–540, 2015.

[24] C. Wang, K. Feng, H. Zhang, and Q. Li, "Seismic performance assessment of electric power systems subjected to spatially correlated earthquake excitations," *Struct. Infrastruct. Eng.*, vol. 15, no. 3, pp. 351–361, 2019.

[25] A. P. S. Golla, S. P. Bhattacharya, and S. Gupta, "The accessibility of urban neighborhoods when buildings collapse due to an earthquake," *Transp. Res. D, Transport Environ.*, vol. 86, Sep. 2020, Art. no. 102439.

[26] S. Li, B. Hu, Z. Hou, and C. Zhai, "A novel method for post-earthquake functional evaluation of city building portfolios," *J. Build. Eng.*, vol. 89, Jul. 2024, Art. no. 109269.

[27] X. Xu and Y. Zeng, "Time-weighted coverage of integrated aerial and ground networks for post-disaster communications," in *Proc. IEEE Wireless Commun. Netw. Conf. Workshops (WCNCW)*, 2020, pp. 1–6.

[28] W. Wang, Z. Sun, and B. Zhu, "Modeling the seismic impacts on communication networks in smart grid," *Int. J. Distrib. Sensor Netw.*, vol. 11, no. 2, 2015, Art. no. 587640.

[29] A. Cardoni, S. L. Borlera, F. Malandrino, and G. P. Cimellaro, "Seismic vulnerability and resilience assessment of urban telecommunication networks," *Sustain. Cities Soc.*, vol. 77, Feb. 2022, Art. no. 103540.

[30] D. Jimenez and A. Medina, "Resilience of a telecommunications network subjected to correlated geographical failures," *Rel. Theory Appl.*, vol. 18, no. 2, pp. 315–326, 2023.

[31] D. Jiménez, J. Barrera, and H. Cancela, "Communication network reliability under geographically correlated failures using probabilistic seismic hazard analysis," *IEEE Access*, vol. 11, pp. 31341–31354, 2023.

[32] A. Du, "Implications of 5G rollout on post-earthquake functionality of regional telecommunication infrastructure," *J. Infrastruct. Intell. Resilience*, vol. 3, no. 1, 2024, Art. no. 100084.

[33] *Propagation Data and Prediction Methods Required for the Design of Terrestrial Broadband Radio Access Systems Operating in a Frequency Range From 3 to 60 GHz*, Rec. P.1410, ITU, Geneva, Switzerland, 2013.

[34] "Radio frequency (RF) system scenarios, Release 17," 3GPP, Sophia Antipolis, France, Rep. TR 25.942 V17.0.0, 2022.

[35] J. Baker, B. Bradley, and P. Stafford, *Seismic Hazard and Risk Analysis*. Cambridge, U.K.: Cambridge Univ. Press, 2021.

[36] B. S.-J. Chiou and R. R. Youngs, "Update of the Chiou and Youngs NGA model for the average horizontal component of peak ground motion and response spectra," *Earthq. Spectra*, vol. 30, no. 3, pp. 1117–1153, 2014.

[37] M. S. Kirçil and Z. Polat, "Fragility analysis of mid-rise R/C frame buildings," *Eng. Struct.*, vol. 28, no. 9, pp. 1335–1345, 2006.

[38] H. Dabiri, A. Faramarzi, A. Dall'Asta, E. Tondi, and F. Micozzi, "A machine learning-based analysis for predicting fragility curve parameters of buildings," *J. Building Eng.*, vol. 62, Dec. 2022, Art. no. 105367.

[39] T. Nishino, T. Tanaka, and A. Hokugo, "An evaluation method for the urban post-earthquake fire risk considering multiple scenarios of fire spread and evacuation," *Fire Saf. J.*, vol. 54, pp. 167–180, Nov. 2012.

[40] C.-H. Liu and H.-C. Tsai, "On the limits of coexisting coverage and capacity in multi-RAT heterogeneous networks," *IEEE Trans. Wireless Commun.*, vol. 16, no. 5, pp. 3086–3101, May 2017.

[41] G. Strang, *Calculus (Open Textbook Library)*. Wellesley, MA, USA: Wellesley-Cambridge Press, 1991.

[42] D. K. Yadav, *Nonelementary Integrals: Indefinite Nonintegrable Functions*. Seattle, WA, USA: Amazon Digital Services LLC, 2023.

AHMET ENES DURANAY (Graduate Student Member, IEEE) received the B.S. degree in electronics engineering from Gebze Technical University, Gebze, Türkiye, in 2014, and the M.S. degree in electrical and computer engineering from Altinbas University, Istanbul, Türkiye, in 2018. He is currently pursuing the Ph.D. degree with Istanbul Medipol University, Istanbul. His research interests include interference management, non-terrestrial networks, centralized radio access networks, peak-to-average power ratio reduction, and disaster management for 5G and beyond radio access technologies. He is a member of the Communications, Signal Processing, and Networking Center.

XHELJA KODHELI (Graduate Student Member, IEEE) received the B.S. degree from the Electronics and Communication Engineering Department, Istanbul Technical University, Türkiye, in 2022. She is currently pursuing the M.S. degree with Istanbul Medipol University, Istanbul, Türkiye. Her research interests include mobility management for NTNs, PHY layer security for NTNs, integrated TN-NTNs, and disaster management for 5G and beyond radio access technologies. She is a member of the Communications, Signal Processing, and Networking Center.

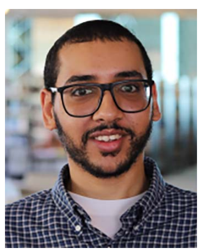

AMR M. ABDELHADY (Senior Member, IEEE) received the B.S. (Hons.) degree in communications and computer engineering from Cairo University, Giza, Egypt, in 2012, the M.S. and Ph.D. degrees in electrical engineering from the King Abdullah University of Science and Technology, Thuwal, Saudi Arabia, in 2016, and 2021, respectively, where he is currently a Postdoctoral Fellow. His general research interests lie in communications theory, signal processing for communications with special emphasis on non-terrestrial networks, and optical wireless communications systems. His specific research areas include UAV communications, visible light communications, green communications, energy harvesting, and reconfigurable intelligent surfaces.

ABDULKADIR CELIK (Senior Member, IEEE) received the first M.S. degree in electrical engineering, the second M.S. degree in computer engineering, and the Ph.D. degree in co-majors of electrical engineering and computer engineering from Iowa State University, Ames, IA, USA, in 2013, 2015, and 2016, respectively. He was a Postdoctoral Fellow with the King Abdullah University of Science and Technology, Thuwal, Saudi Arabia, from 2016 to 2020, where he is currently a Senior Research Scientist with the Communications and Computing Systems Laboratory. His research interests are in the broad areas of next-generation wireless communication systems and networks. He is the recipient of the IEEE Communications Society's 2023 Outstanding Young Researcher Award for Europe, Middle East, and Africa region. He currently serves as an Editor for the IEEE TRANSACTIONS ON COMMUNICATIONS, IEEE COMMUNICATIONS LETTERS, IEEE WIRELESS COMMUNICATION LETTERS, and *Frontiers in Communications and Networks*.

AHMED M. ELTAWIL (Senior Member, IEEE) received the B.S. and M.S. degrees (Hons.) from Cairo University, Giza, Egypt, in 1997 and 1999, respectively, and the Ph.D. degree from the University of California, Los Angeles, in 2003. He is currently a Professor of electrical and computer engineering with the King Abdullah University of Science and Technology (KAUST), where he joined the Computer, Electrical and Mathematical Science and Engineering Division in 2019. Prior to that, he has been with the Electrical Engineering and Computer Science Department, University of California, Irvine, since 2005. He is the Founder and the Director of the Communication and Computing Systems Laboratory, KAUST. He has been on the technical program committees and steering committees for numerous workshops, symposia, and conferences in the areas of low-power computing and wireless communication system design. His current research interests include the general area of smart and connected systems with an emphasis on mobile systems. He received several awards, including the NSF CAREER grant supporting his research in low-power computing and communication systems. He received two United States Congressional certificates recognizing his contributions to research and innovation. In 2021, he was selected as the "Innovator of the Year" by the Henry Samueli School of Engineering, University of California. He is a Senior Member of the National Academy of Inventors, USA.

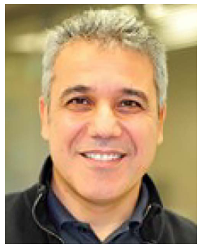

HÜSEYIN ARSLAN (Fellow, IEEE) received the B.S. degree from the Middle East Technical University, Ankara, Türkiye, in 1992, and the M.S. and Ph.D. degrees from Southern Methodist University, Dallas, TX, USA, in 1994 and 1998, respectively.

From January 1998 to August 2002, he was with the Research Group of Ericsson, where he was involved with several projects related to 2G and 3G wireless communication systems. From August 2002 to 2022, he was a Professor with the Electrical Engineering Department, University of South Florida. In December 2013, he joined Istanbul Medipol University to found the Engineering College, where he has been working as the Dean of the School of Engineering and Natural Sciences. In addition, he has worked as a Part-Time Consultant for various companies and institutions including Anritsu Company and The Scientific and Technological Research Council of Türkiye. He conducts research in wireless systems, with an emphasis on the physical and medium access layers of communications. His current research interests are on 6G and beyond radio access technologies, physical layer security, interference management (avoidance, awareness, and cancelation), cognitive radio, multi-carrier wireless technologies (beyond OFDM), dynamic spectrum access, co-existence issues, non-terrestrial communications (High Altitude Platforms), joint radar (sensing) and communication designs. He has been collaborating extensively with key national and international industrial partners and his research has generated significant interest in companies such as InterDigital, Anritsu, NTT DoCoMo, Raytheon, Honeywell, and Keysight technologies. Collaborations and feedback from industry partners have significantly influenced his research. In addition to his research activities, He has also contributed to wireless communication education. He has integrated the outcomes of his research into education which led him to develop a number of courses at the University of South Florida and Istanbul Medipol University. He has developed a unique "Wireless Systems Laboratory" course (funded by the National Science Foundation and Keysight Technologies) where he was able to teach not only the theory but also the practical aspects of wireless communication systems with the most contemporary test and measurement equipment.

Dr. Arslan has served as a General Chair, the Technical Program Committee Chair, the Session and Symposium Organizer, the Workshop Chair, and the Technical Program Committee Member in several IEEE conferences. He is currently a member an Editorial Board for IEEE SURVEYS AND TUTORIALS and *Sensors Journal*. He has also served as a member an Editorial Board for the IEEE TRANSACTIONS ON COMMUNICATIONS, the IEEE TRANSACTIONS ON COGNITIVE COMMUNICATIONS AND NETWORKING, and several other scholarly journals by *Elsevier*, *Hindawi*, and *Wiley Publishing*. He is a Distinguished Lecturer and a Member of Turkish Academy of Sciences